SGX
ACTIVITY REPORT
2017-2018

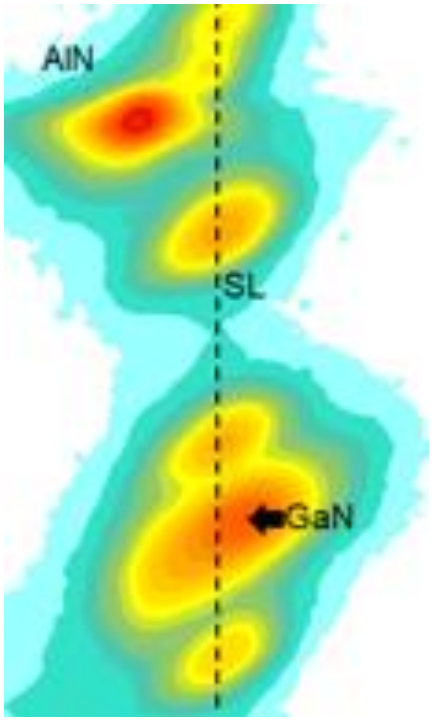

IRIG (ex INAC) X-Ray characterization laboratory

SGX Team

- Edith Bellet-Amalric (1/2 SGX -1/2 Pheliqs/NPSC)
- Alain Farchi
- Arnaud de Geyer
- Stéphane Lequien
- Bernard Mongellaz
- Jacques Pécaut (SyMMES/CIBEST)
- Stéphanie Pouget (resp.)

SGX in a few words

The SGX X-ray characterization laboratory at CEA-IRIG provides access to state-of-the-art equipments, holds trainings in different fields of X-ray characterization (powder XRD, thin film XRD, reflectivity, single crystal XRD, small angle scattering). It offers advice and technical assistance in data collection and data analysis, and is in close connection with the ESRF and ILL Grenoble X-Ray and neutron large scale facilities. In the last years, the lab has developed a strong involvement in energy related research projects.

Two PhD thesis started in November 2017 with a MEM-SGX/SyMMES-STEP co-supervision, one on the structure-properties correlations in hybrid perovskites for photovoltaic applications (Asma Medjahed), and the other one on the investigation of the aging mechanisms in silicon-based Lithium-ion batteries by in-situ and operando scattering techniques (Diana Zapata).

The 2017-2018 period was marked by the arrival of a new D8 ADVANCE powder diffractometer allowing measurements in Bragg-Brentano reflexion configuration with a 15 positions sample changer and in transmission geometry for capillaries and membranes. It is equipped with an Anton-Paar HT600 temperature stage covering a temperature range from 80K up to 600°C.

A GISAXS setup was installed on the SAXS instrument, and a temperature stage up to 400°C developed with SyMMES will be available from the first half of 2019.

Since 2018, the single crystal diffractometer is jointly managed by INAC/MEM/SGX and BIG/LCBM.

The lab opens to all IRIG teams, as well as, under conditions to be discussed, to external users.

Contents

Material synthesis / structuration

Instruments

(Technical resp. B. Mongellaz)

In-Plane/Out-of-Plane diffractometer (Rigaku Smartlab)

Since September 2015 a new X-ray diffractometer Smartlab from the Japanese company RIGAKU was open to users. The versaility of the instrument can adapt to the diversity of samples and problems specific to the field of crystalline layers of high structural quality and also to nano-crystalline objects.

This project was carried out by Institut Néel and INAC with co-funding of the LABEX LANEF. The equipment is managed jointly by the 2 institutes. In 2016 a management agreement was signed by UGA (representing the LABEX), CEA-INAC and CNRS-NEEL. Every year a joint steering committee is held, and once every two years a user meeting takes place.

The main characteristics of the instrument are:

- High brilliance with a 9kW rotating copper anode
- The possibility of carrying out diffraction measurements for which the diffraction vector is either normal to the surface of the sample or in the plane of the sample and more generally the ability to probe along almost any direction of the reciprocal space. For this purpose, the arm carrying the detector has two degree of freedom.
- A modular design for an easy change of diffraction geometry:
  - High resolution mode with a parabolic mirror, 2 monochromators Ge(220) 2 and 4 reflections, a Ge(220) 2 reflections analyzer.
  - Medium resolution with a parabolic mirror and plane collimators
- Two detectors: a punctual scintillator and a 1D strip. This linear detector allows a factor 50 in gain of time for the acquisition of reciprocal space maps.
- A goniometer with a θ–θ configuration (horizontal sample). The motors ω, ϕ, χ, and the 2 degrees of freedom of the detector 2θ and $2\theta\chi$ allow to perform diffraction measurements in and out of plane. An independent double tilt is used for sample alignment.
- An oven that can reach 1100°C under vacuum or under N_2 atmosphere (fix or scanning flux).
- An XY mapping translation stage (± 10 mm in each direction) with an X,Y resolution better than 0.1 mm. It can also be used as an automatic sample changer.

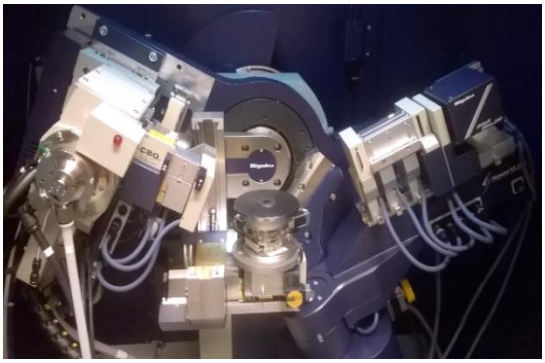

Out of plane

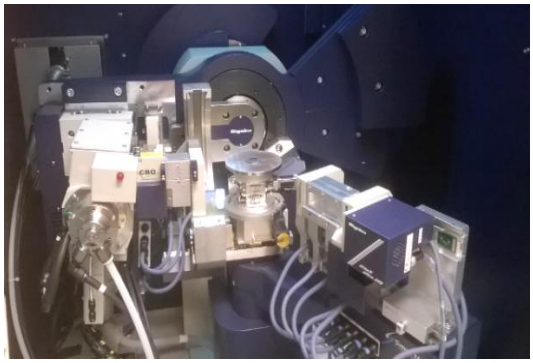

In plane

Thanks to its large versatility, the diffractometer can be used for a broad **variety** of **materials** such as organic/inorganic thin films, epitaxial metal/semiconducting layers, with different geometries: 2D thin-film of a few monolayers or superlattices, but also in 1D nanowire geometry, or 0D like quantum dots or nanoparticles.

Software:

- **Smartstudio 2** : Profile and structure analysis software for diffraction of epitaxial layers (strain, composition, superlattices).

(*resp. E. Bellet-Amalric and S. Grenier from I. Néel*)
(technical *resp. B. Mongellaz and C. Bouchard from I. Néel*)

Small Angle/Grazing-Incidence X-ray Scattering (SAXS / GISAXS)

The X-ray source is a copper rotating anode (Bruker FR591-Nonius) operating at 3 kW with a source size of 200x200 μm^2 and Cu-Kα radiation (λ = 1.5418 Å). The x-ray optics consists into a set of two horizontal and vertical 16 cm long Ni-filtered total reflection mirrors (Kirkpatrick-Baez mirrors) positioned at 180 cm from the x-ray source. The size of the source (200x200 μm^2) and its distance from the x-ray optics (180 cm) provide a low divergence of the x-ray beam (~ 0.05 mrad) which is a key parameter (with the high-brightness) to optimize the SAXS and GISAXS applications.

The beam line is equipped with a set of 4 beam defining slits (close to mirror optics) and a set of 4 anti-scattering slits in front of sample position (Xenocs motorized non-scattering slits). The distance between the two sets of slits is 180 cm thus providing very low-background intensity even at low scattering angle.

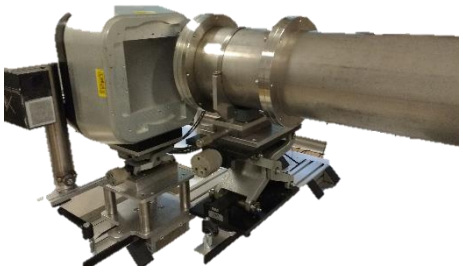

The Detector Vantec 2000

Two different detectors are available. One 20x20 cm^2 large area delay-line ESRF detector, or a 14x14 cm^2 area (Bruker VANTEC-2000) mikroGap® detector. The mikroGap® technology gives a very fine Point Spread Function which allows to measure even weak scattering intensities close to strong diffraction peaks with pixel size resolution of either 70 μm, 140 μm or 280 μm.

In the SAXS mode, the flux on the sample is ~ $3x10^7$ ph/s with a beam size (FWHM) ~ 600x600 μm^2. The sample to detector

distance can be tuned from 20 cm to 400 cm, which corresponds to wave vectors from 10^{-3} $Å^{-1}$ (SAXS domain) to 2 $Å^{-1}$ (WAXS domain).

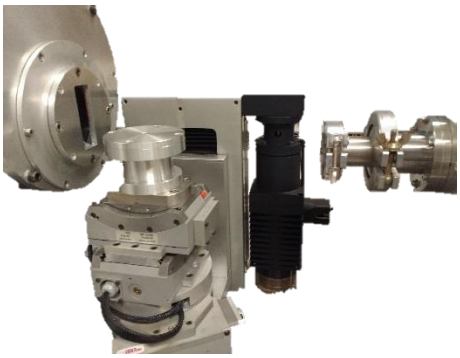

The 4-axis GISAXS setup

New in 2018, the sample chamber has been equipped with GISAXS 4-axis motorization. This equipment assembled from the recovery of precise and functional positioning elements (Rotation, chi, phi, z sample stage) required a specific mechanical and software adaptation in order to be permanently integrated into the sample chamber. This allows a quick change of configuration between SAXS mounting and GISAXS mounting. As for the SAXS configuration, the sample to detector distance is tunable in the range 20-400 cm.

The large sample chamber can accommodate various sample environments as required for *in-situ* or *operando* studies. An automatic acquisition in SAXS experiments is supported by a self-made software associated with a 9 multi-sample stage.

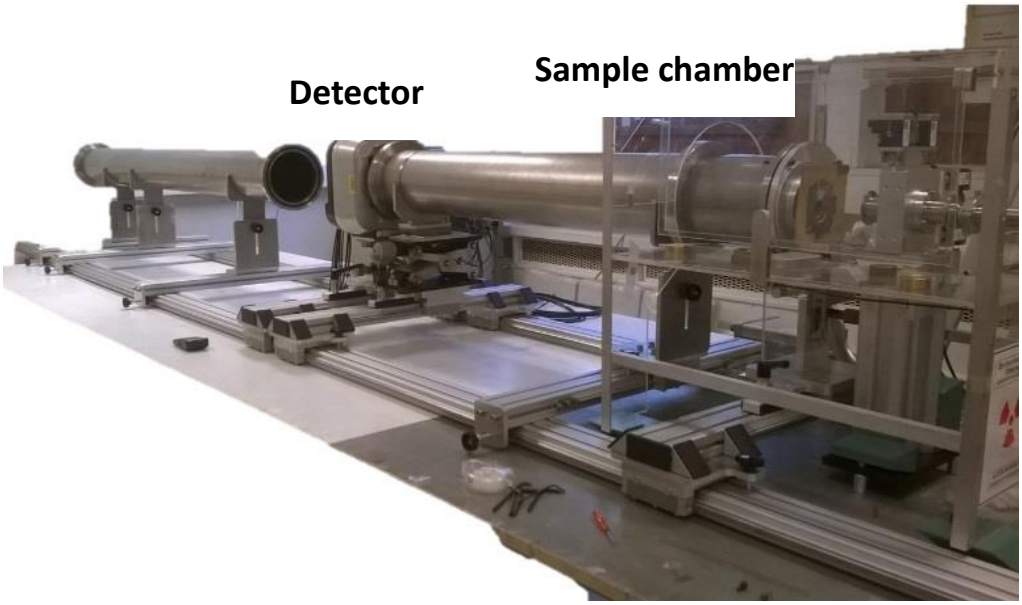

Software:

- **MPAwin**
- **Datasqueeze** (©Paul Heiney, Upenn university) for SAXS measurements
- **Fit2D** (©Andy Hammersley, ESRF)
- **FitGisaxs** (©David Babonneau, Univ Poitiers) for GiSAXS measurements.

(*resp, A. de Geyer and A. Farchi*)

Powder diffractometer (Bruker D8 ADVANCE)

A new D8 ADVANCE powder diffractometer was installed in December 2018. The main characteristics of the instrument are:

- A Cu beam tube
- A linear energy-dispersive LYNXEYE XE-T detector which combines fast data collection with filtering of fluorescence and K_β radiation (energy resolution better than 380 eV).
- A motorized anti-scattering screen (MASS) enables data collection at low 2θ angles.
- A 15 positions sample changer (available in Bragg-Brentano reflexion geometry). (Figure a)
- A fixed or variable divergence slit
- A focusing mirror for transmission geometry for capillary or membrane samples.
- An Anton-Paar HT600 temperature stage which covers temperatures from 80K up to 600°C (Figure b)
- Various sample environments such as an optimized battery cell for *in-situ* or *operando* studies.

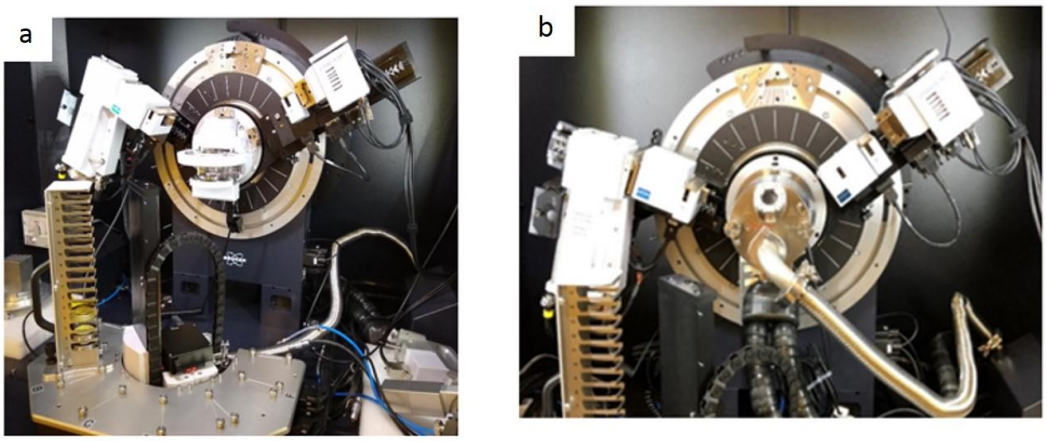

D8 Discover Diffractometer with a 15 position sample changer (a) and an Anton Paar temperature stage (b).

Software:

- **ICDD PDF-4** : Data base for crystalline phase identification from experimental powder pattern.
- **TOPAS** : Profile and structure analysis software for powder and single crystal data XRD.
- **HighScore Plus** : From phase identification to Rietveld analysis.
- **FullProf :** advanced Rietveld refinement.

(*resp. S. Pouget*).

Thin film diffractometer/reflectometer (Panalytical Empyrean)

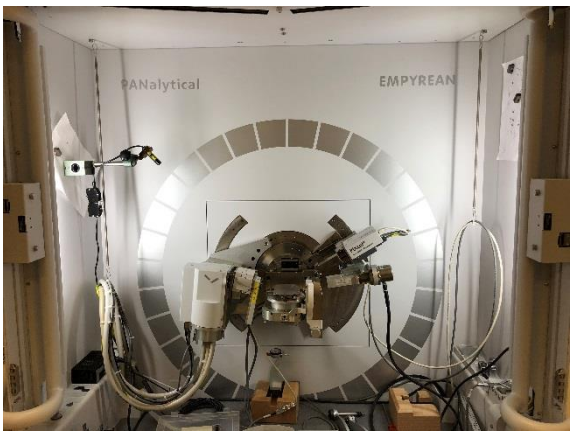

The diffractometer is equipped with a cobalt anode (Co K_α radiation prevents from fluorescence for samples containing iron and cobalt), a chi, phi, z sample stage with RX, RY cradles for thin film alignment and two detectors: a 2D Pixcel detector (255x255 55µm size pixels) and a proportional punctual detector. The Pixcel detector can be used in 0D, 1D or 2D modes.

Measurements can be performed in either diverging, parallel or mixed configuration.

Parallel geometry: Goebel mirror, long plate collimator, proportional punctual detector.

Diverging geometry: Fixed divergence and anti-scattering slits, 2D Pixcel detector.

The diffractometer is used for:

- Determination of the structure, orientation and microstructure (perpendicular and lateral strain and crystallite size) in polycrystalline, textured or epitaxial thin films.
- Thin film reflectivity for thicknesses ranging from a few nanometers up to a hundred nanometers
- Investigation of rough polycrystalline samples (using parallel geometry)

Software:

- **X'Pert Epitaxy**: strain and stoechiometry determination in epitaxial thin films and super-lattices.
- **Motofit, Parratt, GenX**: reflectivity - simulation and refinement.

(*resp. S. Pouget, S. Lequien*).

Single crystal diffractometer (Rigaku XCalibur S)

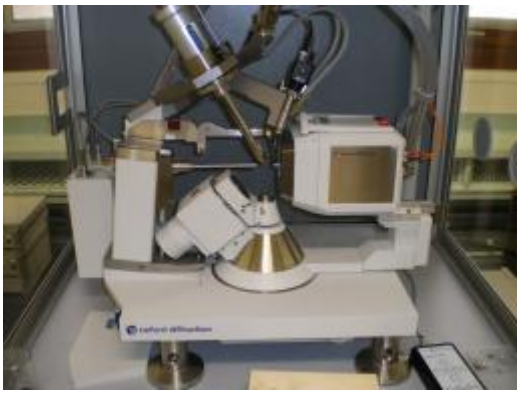

The diffractometer Rigaku XCalibur S (2008) is equipped with a Molybdenium anode and a 4048x4048 pixels CCD detector. A nitrogen sample cooling (T > 100K) is available.

The aim of single-crystal diffraction is the determination of the chemical composition and the atomic positions, without pre-requisite such as the formula.

The obtained information are:

- The nature of the synthetized compound (formula, charge, bond type, absolute configuration …). Results are only typical of the chosen crystal and not of all the species present in the solution. Second,
- The conformation and the 3 dimensional arrangement of the chemical entities inside the crystalline lattice (hydrogen bonds, pi-pi interactions …).

For some studies, only the nature of the synthetized compound is relevant, and, in this case, crystallization is a way to reach it, while for others, interest is not focused only on the motive structure (asymmetric unit) but also on the interactions between the different entities in the cell.

Since 2018, this diffractometer is jointly managed by INAC / MEM / SGX and BIG / LCBM. A steering committee has been set up, which meets once a year.

Software:

- **CCDC/Mercury** : Cambridge data base of single-crystal structures, and visualization.
- **Olex** : interface for structure resolution and finalization of publication files.
- **ShelX 2013** : structure resolution with direct methods, structure refinement.
- **Superflip** : « charge flipping» structure resolution method.
- **Platon** : diffused solvents modelization (SQUEEZE).

(*resp. J. Pécaut INAC, S. Torelli BIG*).

LAUE equipment for single crystals characterization and orientation

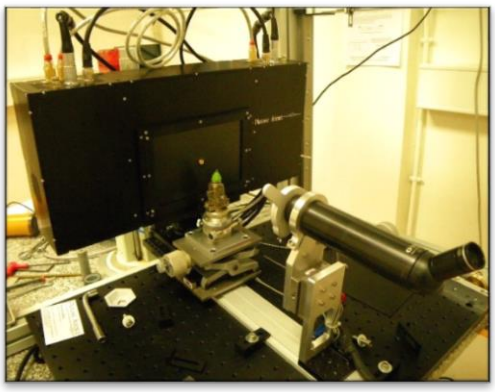

The X ray source is a SIEMENS Kristalloflex generator K760 1.8 kW (45 kV – 40 mA) equipped with a polycapillary XOS™ optic especially designed for focusing and collimating the incident X ray beam.

Laue patterns are recorded with a dual camera from Photonic Science™ through PSL software, and Orient Express, free software for indexation and matrix orientation.

Software:

- **PSL software:** Interface acquisition for high resolution Laue detector (back scattering)
- **Orient Express software:** Laue indexing and orientation of single crystals

(resp. G. Lapertot INAC/PHELIQS/IMAPEC)

Training

SGX holds trainings in different fields of X-ray characterization; they are validated by the physics and chemistry doctoral schools.

- Single crystal diffraction
- Polycrystalline materials
- Thin film characterization – from powder…to single crystal epitaxial layer.
- Epitaxial layers (metal or semiconductors): Thin film and nanostructures
- Small Angle X-Ray scattering

ORZEL. A European Twinning project with Silesia University of Technology (SUT) in Gliwice – Poland.

Coll. INAC/SyMMES/MEM and INAC/SyMMES/STEP

ORZEL (http://orzel-project.com/) was a European project the aim of which was: "Boosting the scientific excellence and innovation capacity in organic electronics of the Silesian University of Technology".

Three partners associated to the SUT laboratory, were the Eindhoven University of Technology (TUE) in Netherlands, the University of Durham (G.B.) and INAC in Grenoble –France. This is a project for which a large number of exchanges of students and scientists have been organized was aimed to introduce Polish colleagues to various technics they did not have in their own laboratory. The project was focused on the fabrication and study of organic PV cells (TUE task), Organic Light Emitting Diodes (Durham) and the characterization of the transport and structure of active materials with advanced technics (INAC) implying D. Djurado (coord. SyMMES) J. Faure-Vincent (SyMMES) and S. Pouget (MEM).

Thus, from February 1st 2016 and 31st January 2019, we welcomed 11 different students and colleagues for a total amount of time of 396 days over 3 years. Accordingly a large amount of this time was devoted to introduce our colleagues to the different X-rays scattering and diffraction techniques available in the SGX laboratory.

Different topics were treated concerning conjugated polymers and molecules as powders, films or thin layers, pushing us to use the whole panel of technical possibilities offered by the SGX.

As an example we will cite the study of electrochemically-modified ITO (Indium Tin Oxide) electrodes involved in neural interfaces for organic bioelectronics. We studied these electrodes by using grazing incidence techniques in order to probe the changes of the ITO electrodes when submitted to electrical potentials either in oxidation or reduction regimes as shown on the figure below.

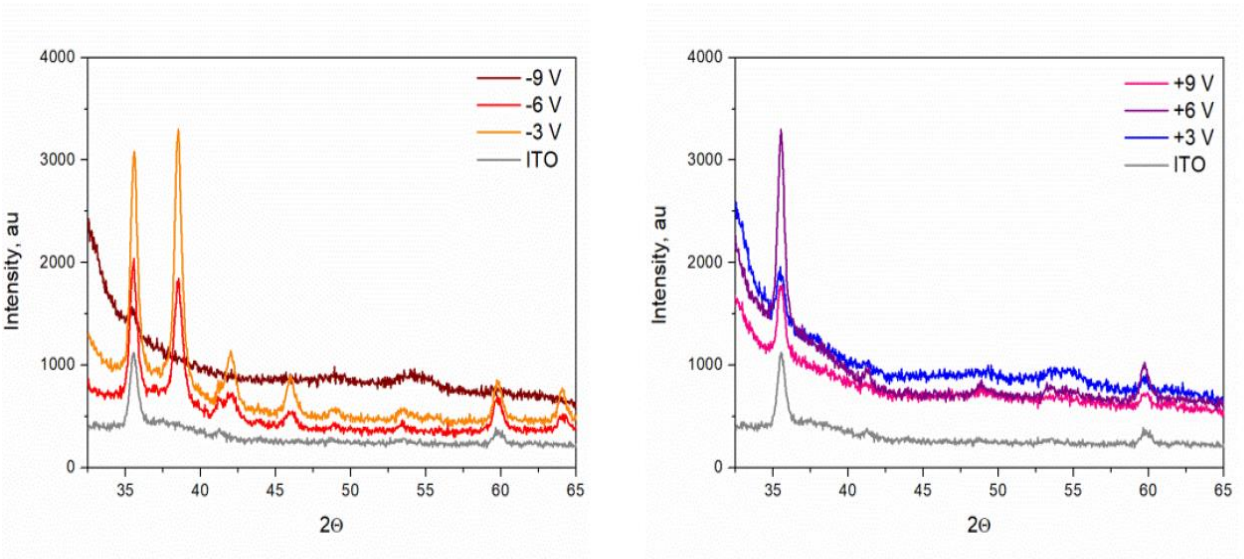

Left: Grazing incidence X-rays measurements on an ITO electrode submitted to different reduction potentials. In this regime we could identify the formation of metallic In and Sn. Right: Grazing incidence X-rays measurements on an ITO electrode submitted to different oxidation potentials. At +6V the phase $In_4Sn_3O_{12}$ *is formed while the starting ITO is in the form* $In_{1.875}Sn_{0.125}O_3$.

Spintronics

2D transition metal dichalcogenides materials

Coll. INAC/SPINTEC/2D Team

Layer-structured transition metal dichalcogenides (TMDs) have drawn much attention recently since they are considered as a new class of semiconducting two-dimensional (2D) materials with thickness-tunable band-gap. In the single-layer, the TMDs offer a unique platform to explore not only the carrier transport in an ultrathin channel but also the control of 2D excitonic systems and the spin valley physics.

WSe_2 on mica

In SPINTEC 2D team we develop Se-based 2D TMDs ($MoSe_2$, WSe_2, $PtSe_2$ etc.) (1 to a few monolayers thick) grown by molecular beam epitaxy on various substrates (SiO_2/Si, graphene/SiC, Pt/sapphire, muscovite etc.). Determining the crystalline orientation, strains and grains size of these layers with respect to the substrate is of great importance to understand TMDs properties. Due to the 2D character of these materials, the grazing incidence in-plane diffraction mode available on the Rigaku-Smartlab apparatus is well suited for such structural studies. For such in-plane diffraction experiments, the incidence angle is optimized close to the substrate critical angle. Various measurements can be done to investigate structural properties:

1) Radial scans ($2\theta_\chi/\phi$) along several directions with respect to the substrate, allow to identify phases and to determine in-plane lattice parameters, strains and crystallite size (Figure 1a)
2) Azimuthal scans (ϕ) performed on Bragg angles found in the radial scans give layer/substrate relative orientation and angular dispersion of the 2D layers.
3) 2D map obtained by scanning both $2\theta_\chi$ and ϕ angles (Figure 1b) provides a more complete view of the reciprocal space, but needs more counting time.

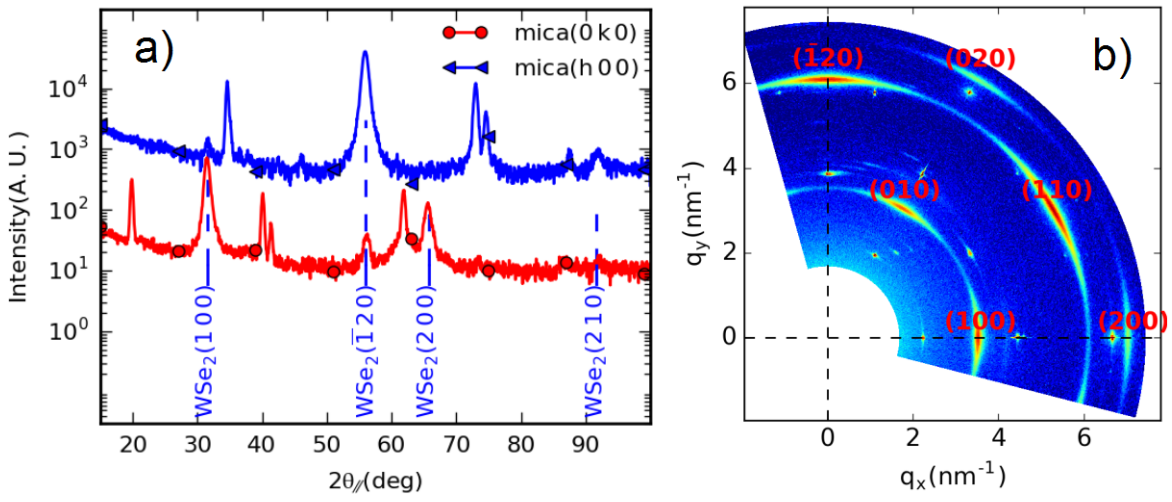

Figure 1 : In-plane diffraction on WSe_2/muscovite (mica). For clarity, only, WSe_2 diffraction peaks are indexed a) two radial scans performed along mica (h00) and (0k0) reciprocal directions. b) Reciprocal space map showing the nearly hexagonal lattice of the mica (sharp dots) and of WSe_2 (indexed arcs features).

An example of this analysis is presented here for WSe_2 grown on muscovite (mica). Muscovite is a natural layered insulating material interesting for transport experiments. WSe_2 is hexagonal, whereas muscovite presents a monoclinic structure C2/m, but its surface lattice is very close to the hexagonal one.

Bi_2Se_3 grown on Ge(111 Effect of doping

Topological insulators (TIs) like Bi_2Se_3 are a class of materials with topologically protected surface states in which spin-momentum locking may enable spin-polarized and defect-tolerant transport. In this work, we achieved the epitaxial growth of Bi_2Se_3 thin films (a few nanometers thick) on germanium, a key material for microelectronics. We aim at combining the long spin diffusion length of Ge with the spin-momentum locking at the surface of Bi_2Se_3.

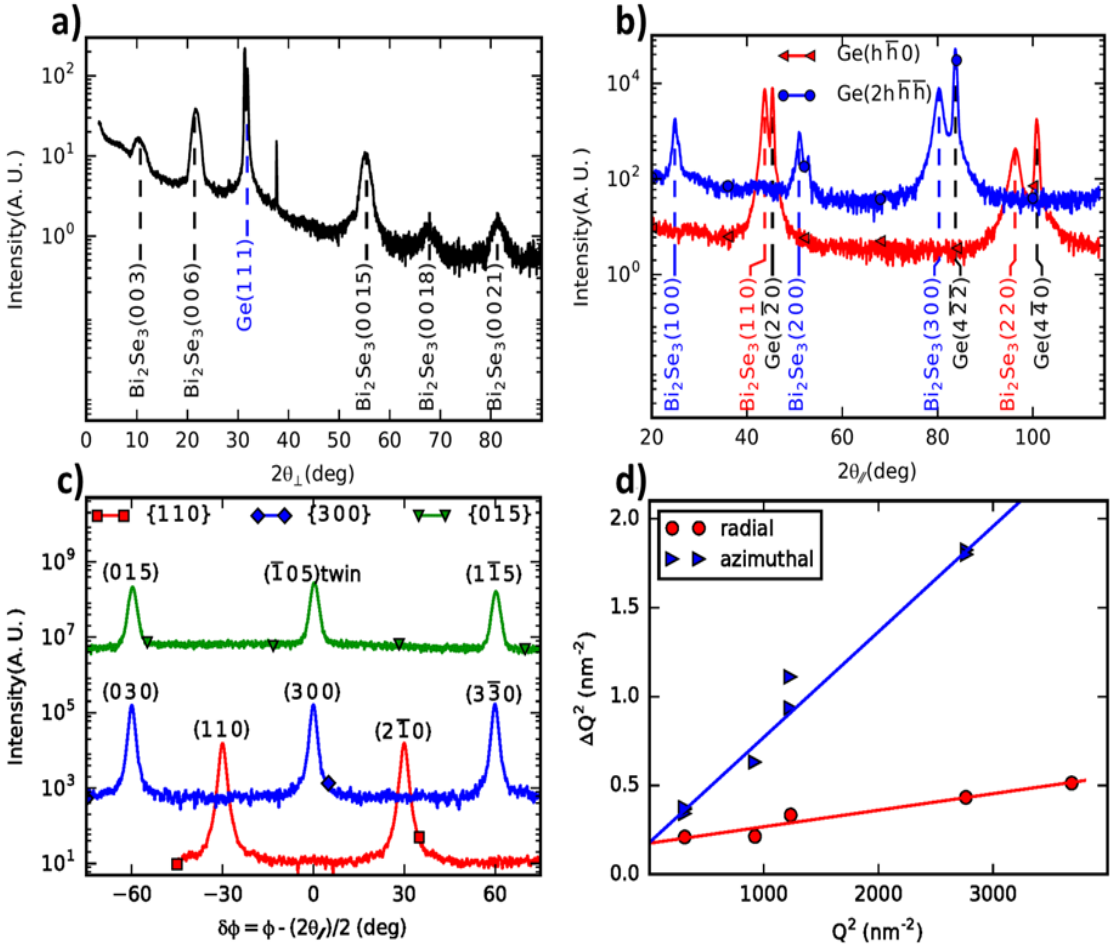

Figure 2 : (a) Out-of-plane ϑ/2ϑ spectrum along Ge(hhh) (b) In-plane grazing incidence radial scans (c) In-plane grazing incidence azimuthal scans for two peaks families {300} and {110}. The azimuthal scan of the {015} reflections was performed using grazing incidence, but with a suitable exit angle (as shown in figure 3). It reveals the presence of twin domains (d) Linear fits of the square of the FWHM of Bragg peaks (in Q units) as a function of the square of the momentum transfer Q.

We performed a thorough structural analysis of the films using in-situ electron diffraction, x-ray diffraction (on the Rigaku-Smartlab instrument) and atomic force microscopy:

- Symmetric out-of-plane θ/2θ diffraction spectra along the Ge(hhh) reciprocal direction (Figure 2a). In addition to the substrate Ge(111) peak, the 5 other peaks can be attributed to the rhombohedral structure R-3m of Bi_2Se_3. They are indexed in the hexagonal unit cell (a=0.4143 nm and c=2.8636 nm) which consists of three Se-Bi-Se-Bi-Se quintuple layers separated from each other by a van der Waals gap. The relative intensities of the peaks are consistent with the calculated structure factors.

- In-plane radial scans (figure 2b) and azimuthal scans (figure 2c) (of the {110} and {300} planes). They confirm the epitaxial relationship between Bi_2Se_3 layer and the Ge substrate: Bi_2Se_3(110)//Ge(1-10).

- Out-of-plane reflections using grazing incidence but with a non-grazing exit angle (see Figure 3). In this geometry, the incident beam is in grazing incidence defined by an angle omega close to the substrate critical angle. In this case, the diffracted beam angle to the surface is larger as schematically represented on the Figure. The momentum transfer can be decomposed in a parallel component, Q// and a perpendicular one, Qz related to the detector positioning angles 2θ and $2\theta_\chi$. The azimuthal angle phi allows rotating the sample (and its reciprocal space) to get coincidence of reciprocal position with the X-rays momentum transfer. This type of experiment is possible thanks to the movement of the detector in the two directions.

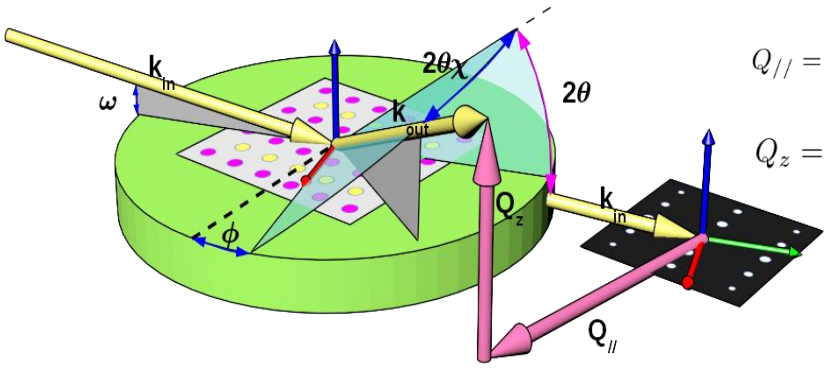

$$Q_{//} = \frac{2\pi}{\lambda}\begin{pmatrix} sin(2\theta_\chi) \\ cos(2\theta_\chi)cos(2\theta-\omega) - cos(\omega) \end{pmatrix}$$

$$Q_z = \frac{2\pi}{\lambda}\left(cos(2\theta_\chi)sin(2\theta-\omega) + sin(\omega)\right)$$

Figure 3: A schematic diagram of the geometries of the out of plane reflection measurement, showing the incident and the output momentum transfer vectors

Pure in-plane measurements cannot exclude twinning which generally occurs due to the simultaneous nucleation of twinned domains on lattice mismatched substrates. Indeed, the ABCAB and ACBAC stackings of the quintuple layer structure give in-plane diffraction peaks {hk0} at the same positions. However, the 3-fold symmetry {015} reflections allows to quantify the degree of twinning. These out-of-plane reflections were obtained using grazing incidence but with a non-grazing exit angle.

The peaks Bi_2Se_3 (015) measured using the configuration discussed above (Figure 2c) show that the film is composed of both twins in equal proportions. This is in agreement with AFM observations showing triangular grains pointing at opposite directions.

- The crystal coherence size >15nm and the in-plane mosaic, 1.4°, where extracted assuming the quadratic dependence between the full width at half maximum (in Q units) and the momentum transfer, Q (Figure 2d).

Ultrathin films Bi/Ge(111)

Bismuth exhibits a series of remarkable electronic properties (very large spin-orbit coupling, long Fermi wavelength, anisotropic effective mass, etc.) that have stimulated experimental and theoretical investigations for decades, in particular in electronic transport studies.

To investigate the spin-charge interconversion we have studied the relation between transport properties and structure as a function of the thickness of Bi thin layers epitaxially grown on Ge(111) [3,4]. During the growth, the bismuth layer exhibits morphological and crystal orientation transitions that were investigated combining in-situ electron diffraction, scanning tunneling microscopy and x-ray diffraction. Bulk Bi has a rhombohedral crystal structure, but the atomic positions appear close to a simple cubic one when observed along (110) orientation.

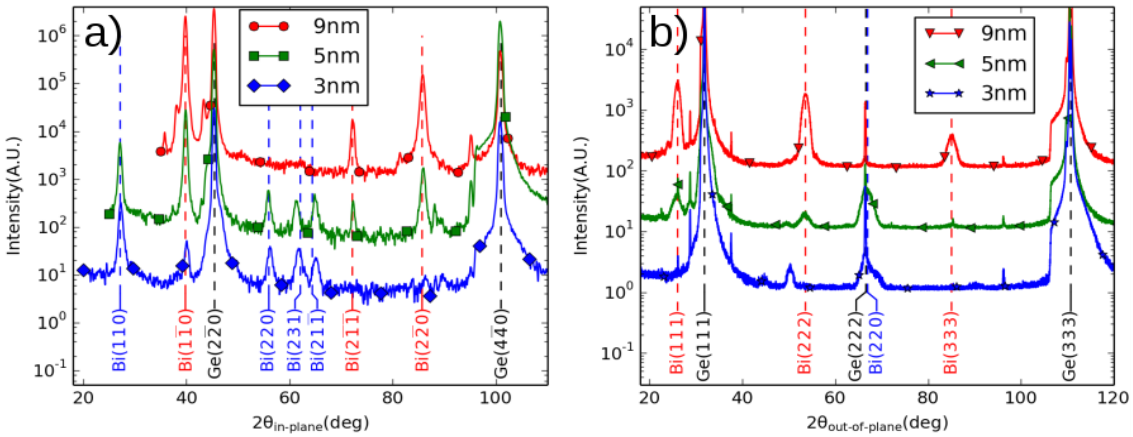

Figure 4 : X-ray diffraction spectra of Bi thin layers grown on Ge(111) for several thicknesses. (a) Grazing incidence in-plane diffraction performed on the Rigaku-Smartlab device (b) out-of-plane diffraction measured using the Panalytical-Empyrean diffractometer. The blue (resp. red) indexes correspond to the PC (resp. HEX) phases.

During the growth, Bi presents 2 structure orientations: the (110)-oriented film named pseudo-cubic (PC) phase and (111)-oriented film named hexagonal phase (HEX).

- Up to t = 3.5 nm, we observe the formation of isolated three-dimensional PC flat nanocrystals or nanoplatelets,
- For 3.5<t<4 nm, the PC nanocrystals start percolating to form a 2D layer,
- For 4<t<5 nm, there is the coexistence of the PC and HEX phases
- Above 5 nm we only observe the single crystalline HEX phase.

These transitions could be observed and finely characterized using both in-plane and out-of-plane X-rays diffraction as shown on Figure 4.

♠ **Millimeter-scale layered $MoSe_2$ grown on sapphire and evidence for negative magnetoresistance**. M. T. Dau, C. Vergnaud, A. Marty, F. Rortais, C. Beigne, H. Boukari, E. Bellet-Amalric, V. Guigoz, O. Renault, C. Alvarez, H. Okuno, P. Pochet, and M. Jamet. *Applied Physics Letters, **110**, 011909 (2017)*

♠ **Magnetotransport in Bi_2Se_3 thin films epitaxially grown on Ge(111).** T. Guillet, A. Marty, C. Beigné, C. Vergnaud, M. -T. Dau, P. Noël, J. Frigerio, G. Isella, M. Jamet. *arXiv:1808.00979*

♠ **Spin-charge interconversion in Bismuth films grown on Ge(111)**. C. Zucchetti, M.-T. Dau , Marty , F. Bottegoni , C. Vergnaud, T. Guillet, C. Beigné, S. Gambarelli, A. Picone, A. Calloni, G. Bussetti, A. Bambrilla, L. Duo, G. Isella, F. Ciccacci, P. Das, J . Fujii, I . Vobornik, M. Finazzi and M. Jamet. *9th JEMS Conference 2018, Mainz, Germany*

♠ **Tuning spin-charge interconversion with quantum confinement in ultrathin Bi/Ge(111) films**. C. Zucchetti, M.-T Dau, F. Bottegoni, C. Vergnaud, T. Guillet, A. Marty, C. Beigné, S. Gambarelli, A. Picone, A. Calloni, G. Bussetti, A. Brambilla, L. Duò, F. Ciccacci, P. K. Das, J. Fujii, I. Vobornik, M. Finazzi, M. Jamet. *Phys. Rev. B* **98**, 184418 (2018) DOI: 10.1103/PhysRevB.98.184418 (*arXiv:1805.01841v1)*

Nanoelectronics

Near- and mid-infrared intersubband absorption

Coll. INAC/Pheliqs/NPSC

Engineering intersubband transitions between confined states in the conduction band have evolved into a promising alternative for the realization of intersubband technologies. Besides planar quantum well structures, nanowires and micropillars are explored as a way to independently control the electrical and the optical device cross section by changing the diameter-to-pitch ratio in the array.

Group-III nitrides (GaN/AlN) offer the possibility to extend the operating range of intersubband devices into the near-IR spectral range, including the 1.3–1.55 µm wavelength window, i.e. for fiber-optic telecommunications. Furthermore, it opens prospects for room-temperature operation of devices (photodetectors, quantum cascade lasers) designed for THz frequencies.

Effect of doping

The n-type doping level is a critical parameter for the performance of ISB devices such as photodetectors or modulators, as the first energy level in the conduction band has to be populated in order to allow transition to higher levels. In planar layers, Si introduces tensile strain in the GaN layers, and high doping with Si lead to surface roughening and crack propagation. The study of high doping levels without causing structural degradation of the material is then crucial.

Using nanowires instead of planar structures as active media in ISB devices can lead to improved performance due to their lower electrical crosssection. Nanowires can have a diameter smaller than the detected/emitted wavelength, and present a large dielectric mismatch with their surroundings. Such features allow engineering the refractive index while maintaining the absorption characteristics of the bulk. Additionally, their large surface-to-volume ratio allows misfit strain to be elastically released, hence expanding the design possibilities of a defect-free active region. Furthermore, three-dimensional (3D) confinement of carriers in nanowire heterostructures might open new possibilities of control of the carrier relaxation time.

We study the effect of doping in both quantum wells and NW heterostructures using the same active region thickness and dopant concentration. We used Si and Ge as dopant. In planar layers, Ge has demonstrated the possibility of obtaining high dopant concentrations, above the Mott density ($10^{19}cm^{-3}$), without surface roughening or crack propagation.

The NWs were synthesized on Si(111) substrates in plasma assisted molecular beam epitaxy (PAMBE). The active region consists of 30 periods of GaN/AlN (2 nm/3 nm) quantum wells (Figure1a). As revealed by SEM all the NWs are vertical but slightly tilted (Figure1b). From a statistical analysis of the microscopy study (Figure 1c and d) we measured an average period of 2.0±0.3 nm for the GaN layer and 3.0±0.3 nm for the AlN.

Both NW and planar heterostructures were analyzed by high resolution X-ray diffraction (HRXRD) using the Rigaku SmartLab diffractometer. Figure 2 presents the θ/2θ scan of the (0002) reflection of all the GaN/AlN heterostructures under study. For the planar structures, a period of 4.8±0.1 nm was measured. For the NWs, although they are tilted and there is a thickness fluctuation from NW to NW, the superlattice signature is clear. The average period extracted from the inter-satellite angular distance is 4.6±0.2 nm for both samples doped Ge and Si (this value is slightly larger than the one obtained locally by microscopy but in the case of HRXRD the average is performed on a cm^2 region).

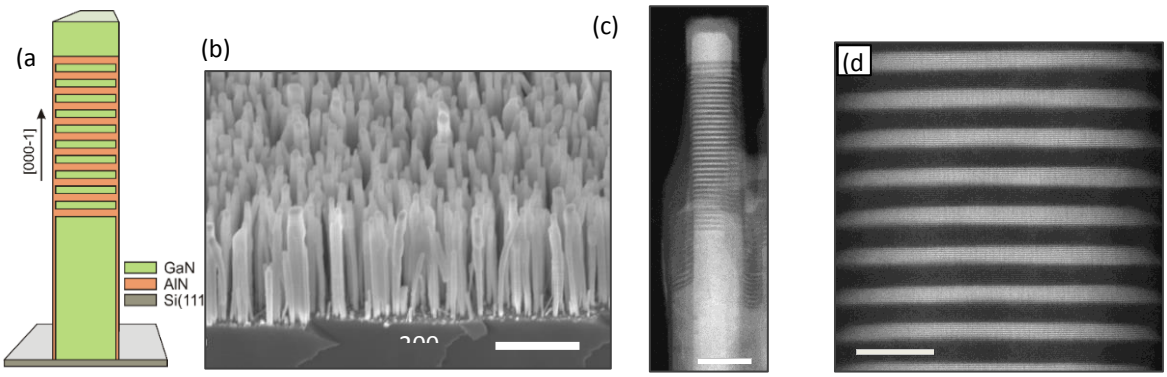

Figure 1 (a) Schematics of the active region in the NW; (b) cross-section SEM images of the Ge doped NWs; (c) and (d) HAADF-STEM images of the same NWs at two different magnifications. Dark/bright contrast corresponds to AlN/GaN

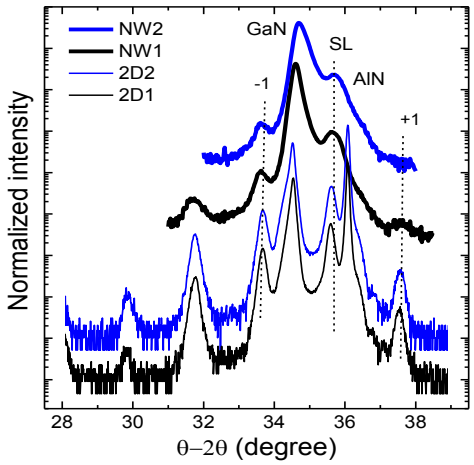

Figure 2: HRXRD θ–2θ scan of the (0002) reflection of the GaN/AlN heterostructures under study. The peak labeled SL corresponds to the main reflection of the GaN/AlN superlattice.

From optical measurements we showed that Both Si and Ge are equally suitable for the fabrication of GaN/AlN quantum wells or NW heterostructures with intraband absorption in the short-wavelength infrared range.

♠ **Intersubband absorption in Si- and Ge-doped GaN/AlN heterostructures in self-assembled nanowire and 2D layers.** A. Ajay, C. Lim, D. Browne, J. Polaczynski, E. Bellet-Amalric, M. den Hertog, and E. Monroy. *Phys. Status Solidi B 254, No. 8, 1600734 (2017) / DOI 10.1002/pssb.201600734*

In top-down GaN/AlN nano- and micropillars

Due to the large lattice-mismatch between GaN and AlN, bottom-up nanowire heterostructures allows low dislocation densities thanks to the elastic strain relaxation at the nanowire surface. However, this advantage comes at the expense of a wire-to-wire inhomogeneity of the superlattice dimensions inherent to the self-assembled growth. As a consequence, the intersubband absorption is spectrally broad when compared to planar quantum wells or quantum dots. Top-down nano- and micropillar arrays are an interesting alternative, where homogeneity is no longer a problem, but there is a risk associated to the damage generated during the etching process.

GaN/AlN quantum well superlattices were etched into nano- and micro-pillars (Figure 3) in order to investigate the influence of this process on the structure and strain-state, on the interband emission and on the intersubband absorption.

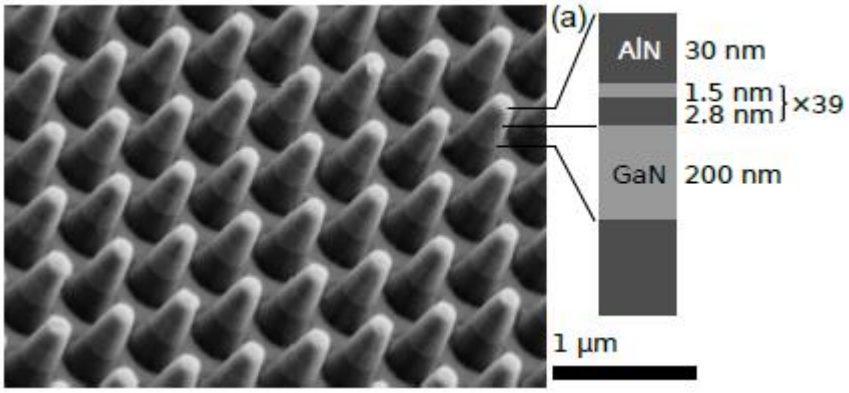

Figure 3. Bird's-eye view SEM image and sketch of the layer stacks for NIR sample etched into pillars with d =0.2 µm

The structural characteristics of the GaN/AlN superlattice and the influence of the top-down processing were investigated. High-resolution x-ray diffraction (XRD) of the as-grown and processed samples was performed using the Rigaku SmartLab X-Ray diffractometer system.

Figure 4(a) shows ω–2θ profiles around the (0002) reflection for the as-grown and etched into nanopillar arrays. In the diffractogram of the as-grown material, the angular location of the reflection from the GaN buffer layer confirms that it remains partially strained (35%) by the AlN substrate.

The determination of the strain state of the superlattice was obtained with the reciprocal space map around the (-2025) (Figures 4(b) and (c)). Several satellites of the superlattice reflection can be identified, at an intermediate Qx vector between the AlN substrate and the GaN buffer layer. The strain state of the superlattice which is relaxed is therefore not modified by the etching. Only the reflection from the GaN buffer layer exhibits a drastic shift, consistent with the observations in the ω–2θ scans. This behavior indicates that the strain state of the superlattice is decoupled from the strain state of the underlying GaN layer.

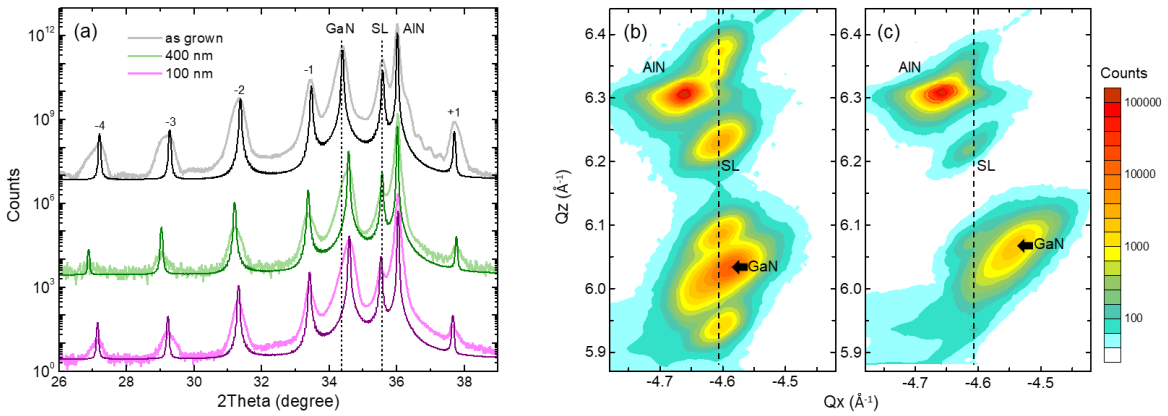

Figure 4. (a) XRD $\omega - 2\theta$ scans around the (0002) reflection of the as-grown sample and etched into pillars with d = 0.4 and 0.1 μm. Superimposed are the simulated profiles. Additionally, reciprocal space maps around the (-2025) reflection are shown for sample NIR (b) as-grown and (c) etched into nanopillars with d = 0.1 μm.

In line with XRD results, the PL emission of the superlattice does not show any spectral shift for the processed samples. Only at room temperature, the non-radiative recombination at the pillar sidewalls has a moderate effect on the PL intensity. Concerning the infrared absorption, the magnitude and linewidth of the intersubband absorption is preserved in spite of the low filling factor even when 80% or 90% of the material is etched away. In fact, by optimizing the pillar dimensions and spacing, the pillar detectors can be expected to outperform planar detectors, while at the same time lifting selection rules concerning the polarization of the incoming light.

♠ **Near- and mid-infrared intersubband absorption in top-down GaN/AlN nano- and micropillars**
J. Lähnemann. D. Browne; A. Ajay, M. Jeannin, A. Vasanelli, J.L. Thomassin, E. Bellet-Amalric, E. Monroy
Nanotechnology doi: 10.1088/1361-6528/aaef72

Epitaxial orientations and 3-phase metal-insulator transition in a VO_2 420 nm-film on Al_2O_3 (0001)

Institut Néel/PLUM (coll. SmartLab)

The metal-insulator transition (MIT) in VO2 has raised interest in the field of strongly correlated electron physics as well as for device integrations like optical filters, memory materials, or thermochromic windows. Optimizing the operating conditions of VO_2 thin films relies on the tuning of its metal-insulator transition, in particular its temperature at 68 deg. in bulk, via doping and substrate strain. However, the insulating monoclinic state of VO_2 has several polymorphs with very close energies, and the literature report different in-plane growth orientation related to different

macrostructures and transport properties. This variety of results requires further detailed high resolution study on the crystallographic phases and the epitaxial relationships.

The Smartlab diffractometer was used in out of plane and in-plane configurations using the Anton-Paar oven up to 100°C.

- We were able to follow the structural transitions, which involves an intermediary phase. Figure 5a shows the specular (400) reflection against temperature. We clearly observed three phases. The low temperature ``M'' (Monoclinic) phase does not directly transform into the metal ``R'' (Rutile) phase, like in the bulk. The transition actually involves a third ``Mx'' phase, which surprisingly persists to high temperatures (Figure 5b).

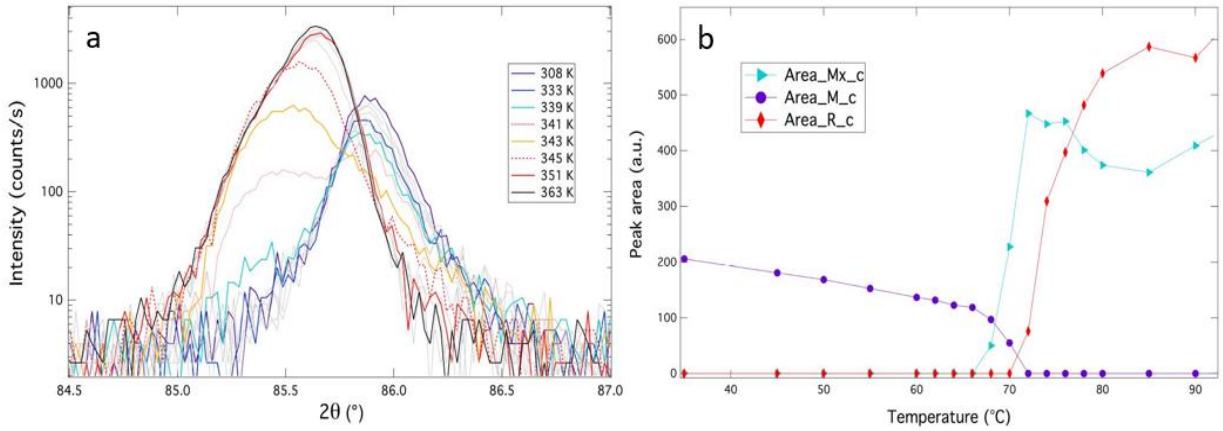

Figure. 5: (a) Specular (400) reflection, versus temperature, resolved using the monochromotized beam; (b) The intensity of the (400) reflection was fitted to a three Gaussians whose intensities are interpreted as coming from three different phases, successively or concomitantly present in the film.

- We were able to unravel the two in-plane orientations reported in the literature. Figure 6a shows the in-plane reciprocal space map, leading to the determination of one of two in-plane orientations of the films on the alumina substrate (Figure 6b). The map was taken with a grazing scattering geometry in order to increase the signal from the film's reflections with in-plane components only.

These results are fed back to our colleagues, who fine tune the growth parameters seeking a decrease of the transition temperature without compromising on its high contrast in transport and optical properties.

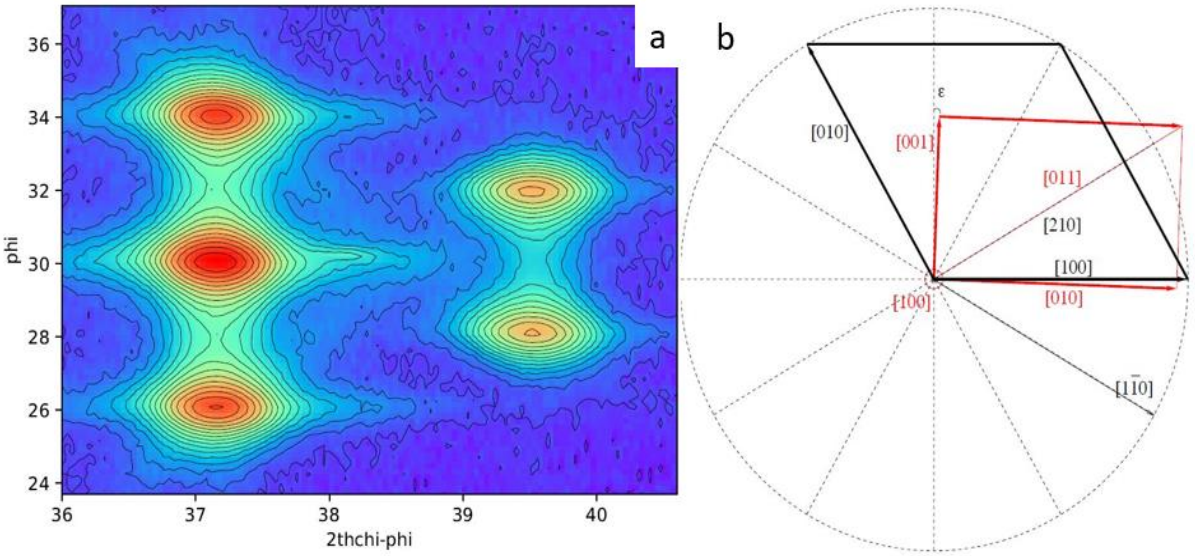

Figure 6. (a) in-plane RSM near the (110) reflection of the substrate, showing the (011) and (020) equivalent reflections from the VO_2 film; (b) Direct space representation of the epitaxial relationship of the VO_2 film rutile unit cell (red, {100}-plane) on the alumina substrate (black, {001}).

Superconducting nanowire single photon detectors based on NbTiN thin films on III-nitrides

Coll. INAC/Pheliqs/NPSC

Superconducting-nanowire single-photon detectors (SNSPDs) have undergone rapid development, and can now outperform single-photon avalanche diodes. Use of GaN and AlN as carrier wafer presents interesting advantages: they are almost lattice matched with NbTiN, which is widely used as superconductor material for SNSPDs, they are transparent from their band gap to 6 µm (UV to mid-IR applications) and their strong electro-optic effects open possibility of on-chip polarization control.

The impact of III-nitride substrates on the crystalline properties of ultra-thin (11 nm) films of NbTiN films deposited by reactive magnetron sputtering was studied. Various substrates were considered: a 1-µm-thick AlN-on-sapphire, GaN/AlN (650 nm/1 µm) heterostructure on sapphire, and free-standing 350-µm-thick Ga, neither non-intentionally doped (n-type conductive) or Fe-doped (semi-insulating).

Thicknesses of NbTiN layers were determined precisely using X-ray reflectivity. Examples of these measurements are illustrated in Figure 7, together with fits using the GenX software. For all the samples, fits confirm total layer thicknesses around 11 nm.

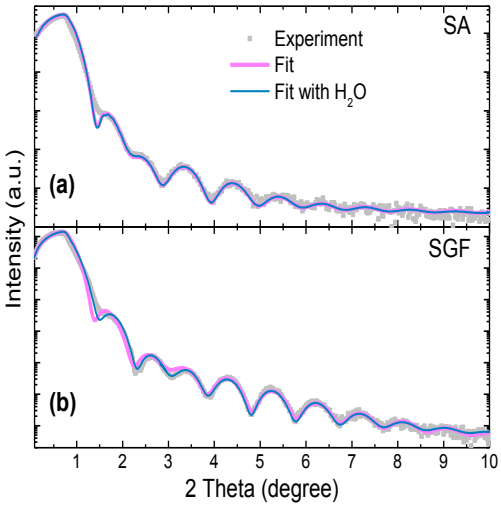

Figure 7. X-ray reflectivity of (a) the NbTiN film on AlN-on-sapphire (sample SA), and (b) the NbTiN film on GaN:Fe (sample SGF). Grey squares are experimental measurements and the solid lines are fits generated with the GenX software. Note that in the case of SA, fits with and without H_2O wetting layer are

Getting a good agreement with the experimental results requires assuming a multilayer structure consisting of:

- a bottom NbTiN layer (~ 8.45±0.45 nm, with ~ 12% Ti in the layer)
- capped by an NbTiNO layer (~ 2.1±0.2 nm, with ~ 17% of nitrogen replaced by oxygen)
- and by a mixture of Nb_2O_5 and TiO_2 (less than one atomic layer, keeping the same Nb:Ti atomic ratio as for the NbTiN layer).

Post-growth oxidation and Nb_2O_5 and TiO_2 demixing are known to occur in NbTiN thin films, but experiments as a function of time show a saturation so that it remains a surface phenomenon. Furthermore, due to the hydrophilic nature of the material, a further improvement of the fit is observed when assuming the presence of a H_2O layer at the surface (see Figure 7a).

From diffraction data, NbTiN layers are (111)-oriented, fully relaxed, and they keep an epitaxial relation with the substrate. Twin domains rotated by 60 degrees are present. High Resolution Transmission Electron Microscopy (HRTEM) images along both [11-20] and [10-10] zone axis of the III-nitride substrates confirm the nominal crystallographic orientation of the substrates, and the establishment of NbTiN(111) [2-1-1] || (Al,Ga)N (0001) [10-10] and NbTiN(111) [2-1-1] || (Al,Ga)N(0001) [01-10] epitaxial relationships, as previously observed in the case of NbN layers.

♠ **Maximizing the efficiency and the polarization-insensitivity of microcavity-enhanced SNSPDs**, L. Redaelli, G. Bulgarini, S. Dobrovolskiy, S. Dorenbos, A. Mukhtarova, N. Tsivadaris, D. Hazra, S. Lequien, F. Duclaroir, V. Zwiller, E. Monroy and J.M. Gérard, Workshop on Nanowire Superconducting Single-Photon Detectors, Lorenz Center, Leiden, The Netherlands (2016)

♠ **Polarization-insensitive fiber-coupled superconducting-nanowire single photon detector using a high-index dielectric capping layer,** A. Mukhtarova, L. Redaelli, D. Hazra, H. Machhadani, S. Lequien, M. Hofheinz, J.-L. Thomassin, F. Gustavo, J. Zichi, V. Zwiller, E. Monroy, and J.-M. Gérard, *Optics Express* ***26,*** *17697-17704 (2018), https://doi.org/10.1364/OE.26.017697*

♠ **Improvement of the critical temperature of NbTiN films on III-nitride substrates,** H. Machhadani, J. Zichi, C. Bougerol, S. Lequien, J.-L. Thomassin, N. Mollard, A. Mukhtarova, V. Zwiller, J.-M. Gérard and E. Monroy, *Supercond. Sci. Technol. (2018) (accepted manuscript, DOI: 10.1088/1361-6668/aaf99d).*

X-ray characterization of superconducting silicon thin films doped with boron

Coll. INAC/PHELIQS and C2N-Orsay

Superconducting devices have shown their great potential, ranging from detectors for astrophysics up to a single photon level detection to very sensitive magnetic sensors with SQUID's. They also play an important role in quantum information which is another promising and growing field of research. So far, the most advanced circuits for quantum computing are based on superconducting qubits and many efforts have been made to increase the number of qubit operations that can be executed within the quantum time. However, the quality of the underlying material must also be addressed as it can be an important source of decoherence for quantum devices. In that quest, superconducting Si:B discovered in 2006 can address all of these challenges at once as the technology is the most mature one for nanoelectronics and for which extremely high quality material can be used so far.

Different superconducting films have been obtained by heavily doping Si or silicon-on-oxide (SOI) with B atoms using 2 techniques:

- the Gas Immersion Laser (GILD) and
- the Pulsed Laser Induced Epitaxy (PLIE).

The GILD technique consists of shining laser pulses (XeCl 308 nm laser with 25 ns pulse duration) at the surface of a wafer on top of which molecules of BCl_3 have been previously chemisorbed. During a laser pulse, Si melts over a thickness and a time that depend on the energy density of the laser. Meanwhile, the atoms diffuse very rapidly into the melted phase while chloride atoms are expelled. At the end of each laser pulse, B atoms are incorporated in substitutional sites as the Si:B layer is epitaxially grown over Si. The number of atoms introduced at each laser pulse is very reproducible and equals 1.2×10^{14} cm^{-2}. To increase the amount of the dopants, the overall procedure is repeated (typically 10 to few hundred times) to reach active concentrations up to 11% at. This high level of concentration, larger than the solubility limit of B in Si ($\simeq$1% at), can be achieved thanks to the rapid liquid/solid phase transition that quenches the atoms into the crystalline phase.

The PLIE technique is used in case of SOI substrates. Prior to annealing, layers are initially preimplanted with dopants which yield to the final achievable concentration. Consequently, a very few number of laser shots (usually one to five) are necessary to get epitaxially layers in comparison to the GILD requiring repeated cycles (up to 200-300).

The surface area illuminated by the laser beam is 2 mm × 2 mm. One wafer can then contains up to 36 samples grown with different laser energies or number of pulses. X-ray diffraction experiments were performed to estimate the B concentration and the thickness of the doped layer. Experiments were performed on the SmartLab diffractometer. An XY mapping translation stage (± 10 mm in each direction, X,Y resolution better than 0.1 mm) was used for that purpose as an automatic sample changer. Samples have been automatically aligned after each X-Y movements.

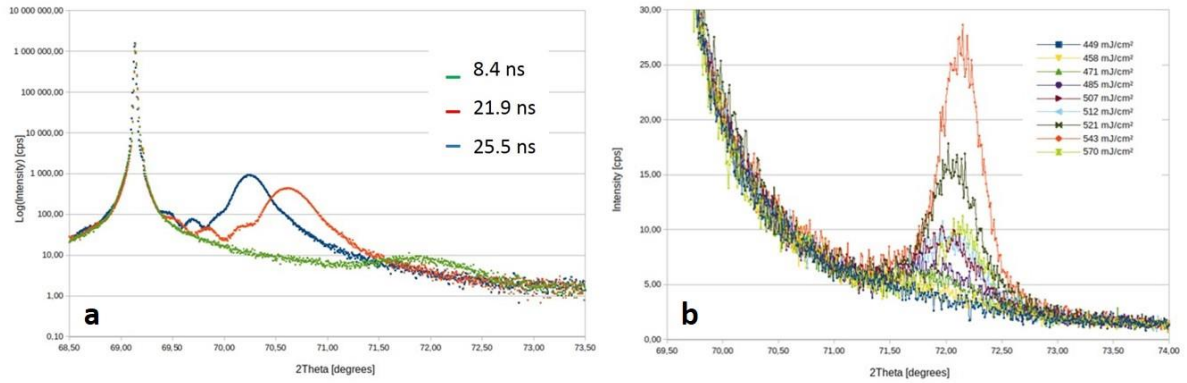

Figure 8 : (a) Evolution of the Si:B (004) x-ray diffraction peak versus melting time. Note that Si:B diffraction peaks move towards low angle values synonym of an evolution of the B concentration – (b) X-ray diffractogram around Si:B (004) versus laser energy densities (melting times) for a B doped SOI substrate .

Representative X-ray diffractograms obtained for different kinds of substrates are displayed in Figure 8a (Si substrate, GILD Technique) and Figure 8b (SOI substrate, PLIE technique). Intensities are plotted versus diffraction angles.

Intensity oscillations between Si and Si:B diffraction peaks can be observed (figure 8) when the density of the laser (melting time) reaches a threshold, the number of laser shots (40) being constant. The more the laser density step is small, the more the threshold can be defined precisely. When the melting time reaches 21.9 ns, the Si:B layer can then be assimilated to a diopter and interactions with X-rays give rise to oscillations from which the thicknesses can be deduced (35 and 46 nm respectively to 21.9 and 25.5 ns melting times).

As already mentioned, in PLIE, one laser shot can homogenized preimplated SOI:B. A diffraction peak can be observed from 470 mJ/cm2 until the highest density delivered by the laser. Nevertheless, whatever the laser density, rough interfaces prevent a trusted determination of the layer thickness. Estimations from the widths of SOI:B diffraction peaks yield to thicknesses varying from 15 to 30 nm depending on the laser energy density.

Pyroelectric thin films elaborated by sol-gel for IR detectors

Coll. LITEN/DTNM, INAC/MEM

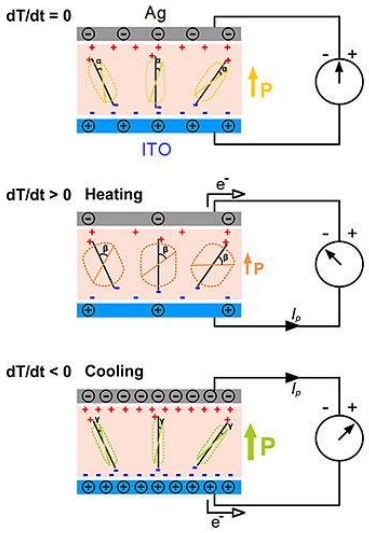

Figure 1: Schematic view of a pyroelectric capacity

Pyroelectric thin films are the topic of current research due to their wide range of applications in thermal IR detectors, sensors, and energy harvesting. Figure 1 displays a schematic view of a pyroelectric capacitor. When the temperature T is constant, the current is null. On the contrary, when T increases, a charge displacement occurs and generates a current. During cooling, the current runs in the opposite direction.

Most of the used pyroelectric materials like the PVDF (PolyVinyliDene Fluoride) have serious limitations such as low pyroelectric coefficient, difficulty of integration and aging over time. Hence, inorganic pyroelectric materials with high pyroelectric coefficient are studied. Such thin films are elaborated by the sol-gel technique, which has several advantages: low material consumption, deposit on large surfaces, even flexible and simplicity. For example, Barium Strontium Titanate (BST) is promising given its high pyroelectric coefficient in bulk as in thin films, its low loss tangent and high figure of merit. BST films are deposited by spin-coating onto a Pt/SiO_2/Si substrate.

X-ray measurements were performed in order to determine the different crystalline phases in the films. Electric (capacitance, resistance, and pyroelectric) measurements are also performed in order to study the pyroelectric behavior of the films. The structural characteristics of the films will be linked to the pyroelectric properties.

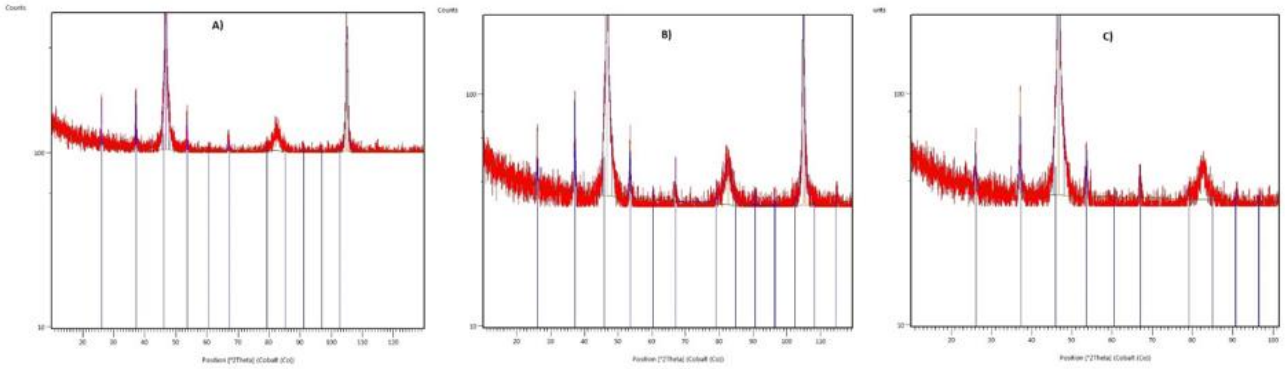

Figure 2: XRD patterns of $Ba_xSr_{1-x}TiO_3$ thin films. Seven layers were successively deposited for a total thickness of 350 nm. The as-spun films were annealed at 600 (A), 700 (B) and 800°C (C).The peaks at 46° and 82° correspond to Pt(111) and Si(400). The vertical lines indicate the peak positions expected for the $Ba_xSr_{1-x}TiO_3$ tetragonal P4mm crystalline phase taken from file 04-009-3218 and 04-009-3220 of the ICDD PDF-4 database.

This work is done in the framework of a LITEN/INAC thesis.

Energy

Thermotropic ionic liquid crystals (TILCs) as lithium-ion battery electrolytes

Coll. INAC/SyMMES,LITEN/DEHT

Lithium-ion batteries (LIBs) are nowadays the power source of choice for portable electronic devices, such as smartphones or laptops, and are steadily gaining momentum in the field of electric vehicles (M. Armand et al., Nature, 451 (2008) 652). However, conventional LIBs are subject to practical challenges such as substantial enhancements of their energy and power density as well as their safety. As the latter aspect directly derives from the flammable liquid organic electrolytes, extensive research efforts are directed towards the development and optimization of alternative solvent-free solid electrolytes (D.T. Hallinan *et al. J. of the Electrochemal Society*, 160 (2013) A464). In this context, INAC/SyMMES and LITEN teams have developed a new generation of thermally stable, thus, intrinsically safer solid electrolyte with covalently bonded anionic functions (single-ion conductivity), showing liquid-crystalline behavior (see Figure1).

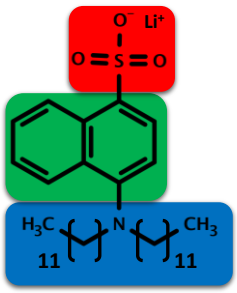

Figure 1. Thermotropic Ionic Liquid Crystal (TILC), labeled C12-Li$^+$.

These electrolytes allow to overcome charge accumulation and thermal runaway leading to the ignition of currently utilized liquid organic. The alkyl-chain length was varied (8-16) to analyze their impact on the liquid crystalline behavior and on the ion transport properties which were investigated through a multiscale approach combing electrochemical impedance spectroscopy (EIS) and Quasi Elastic Neutron Scattering (QENS).

Temperature dependent SAXS spectra of these new electrolytes were recorded in the laboratory in order to identify the different mesophases and their transition temperatures (samples in capillary between 25 and 155°C) (Figure 2a and 2b).

The observed peaks are rather narrow; this is a clear signature for a well-defined nanostructure of the sample in the explored temperature range. The d-spacing ratios are indexed to reflections of a rectangular columnar (Colr) phase for alkyl chain length C12 (Bragg spacings 38 Å and 30 Å) and C16 (Bragg spacings 44 Å and 37 Å). In other words, this new family of ionic liquid crystal self-organizes along a columnar axis (Figure 3b and c). For C8, a lamellar phase was obtained (Bragg spacing: 32 Å).

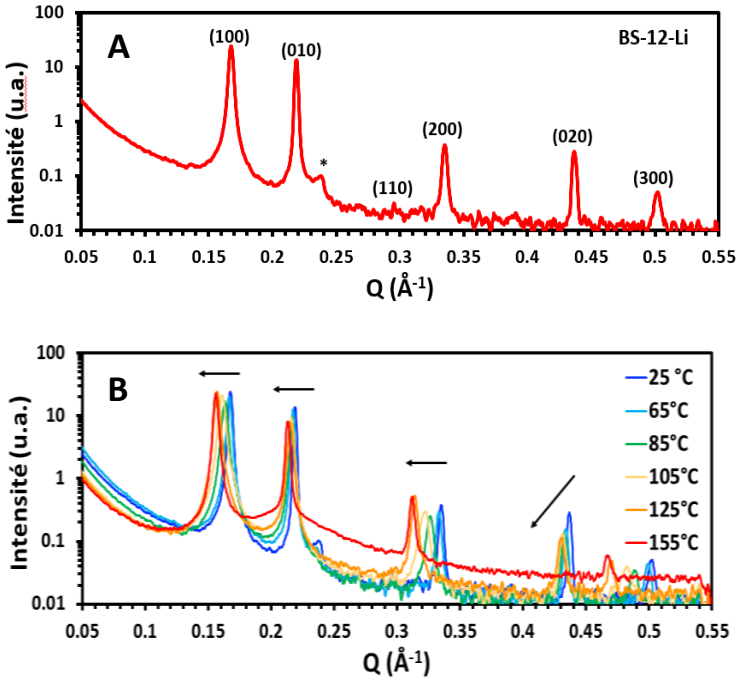

Figure 2 (a) SAXS of C12-Li⁺ recorded at room temperature. (b). Temperature-dependent SAXS of C12-Li⁺.

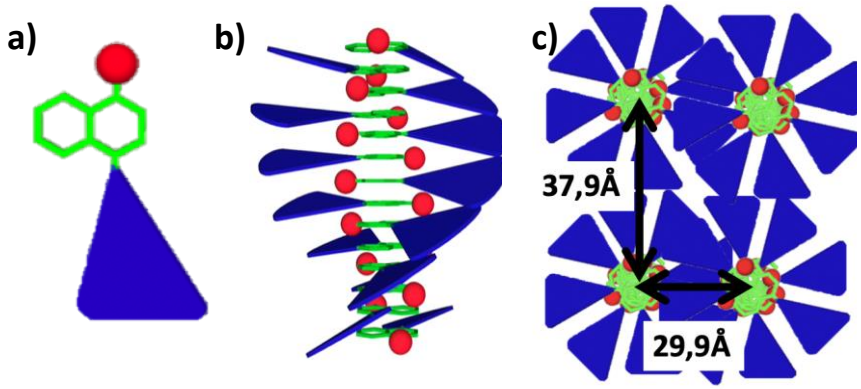

Figure 3. Sketches of (a) the TILC architecture, (b) the molecular stacking into column,(c) supramolecular organization of the columns into Colr mesophases.

The observed structures promote efficient ion transport and suitable thermal and electrochemical stability. The ionic conductivities and the battery performances at high temperatures are promising.

This work is a part of a transversal thesis between INAC and LITEN (Laurent BERNARD, 1st price winner of YESS Award 2018, Réseau RS2E – Batteries Event, October 2018 (Nice - France). *Oral*.).

♠ **Self-assembled liquid-crystalline single-ion conductors for lithium battery electrolytes**. L. Bernard, D. Bresser, P. Rannou, H. Mendil-Jakani, L. Picard, S.Lyonnard, *18th International Symposium on Polymer Electrolytes, ISPE 2018, Yokohama-Japan. Oral.*

Platinum nanoparticles recycling from fuel cells with ionic liquids.

Coll. INAC/SyMMES, LITEN, LETI, C2P2, Univ. Lyon

The cost of a Polymer Electrolyte Membrane Fuel Cell (PEMFC) comes mainly from the platinum nanoparticles (Pt-NPs) which are used as catalyst. It represents 40% of the stack price for a large-scale production (*James et al. 2017 update. Report to the DOE Fuel Cell Technologies Program*). To reduce their cost, it is crucial to be able to produce cheap cells which could compete with fossil energy. To reach this goal, one way is the recycling of platinum. For now, Pt is mainly recycled by the use of calcination steps followed by its dissolution in a mixture of strong acids (aqua regia) (*Duclos, L., et al., Hydrometallurgy 160, 79-89 (2016)*). In the case of PEMFC, the burning of the PEM emits hydrofluoric acid (HF), which makes the waste management complicated. Most of the study makes incremental changes by using less harmful acids, lowering the temperatures or avoiding the HF production but this is not sufficient.

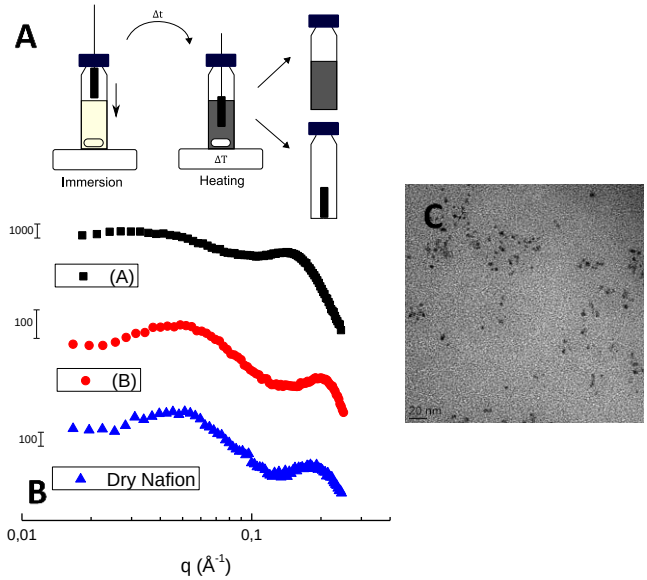

Figure 4:.
***A**. Protocol for the immersion of electrodes in ILs;*
***B**. SAXS profile for a. dry Nafion,*
Nafion membrane immersed in IL(A)
Nafion membrane immersed in IL(B)
Dry Nafion;
***C**. TEM picture of Pt-NPs stabilized in an IL after treatment of the catalyst layer.*

The purpose of this study is to propose a breakthrough approach by avoiding the step of the dissolution of Pt by the extraction from the membrane and the stabilization of Pt-NPs by ionic liquids (ILs) (*Balva, M., et al., ChemSusChem 10, 2922-2935 (2017)*). These solvents, which are salts in a liquid state under 100°C, can stabilize NPs (*Dupont, J., et al. J. D.. Chem. Soc. Rev. 39, 1780 (2010)*). They have a very low vapor pressure and are stable in a wide range of temperature. Moreover ILs are smart solvents: they can be designed for a wide range of applications. These properties make them recyclable and adapted for the recovery of NPs.

The work was focused on the choice of the IL able to penetrate inside the catalyst layer, extract the Pt-NPs and stabilize them. The electrode was immersed in the ILs for a specific time and temperature (Figure 4A). The influence of these parameters was firstly investigated. Twelve ILs and an organic solvent as model (dimethylsulfoxide) were then compared in the same experimental conditions. The ILs were chosen based on their H-bonding ability, viscosity and molar volume. From these results it was possible to give insights in the type of cations and anions required for the Pt extraction. SEM

characterizations gave indications on the delamination and possible expansion of electrodes; EDX and ICP-OES analysis could give quantitatively and qualitatively the efficiency of the Pt extraction. Finally, from TEM analysis we were able to obtain some characteristics of Pt-NPs dispersed in the liquids. To complete this study and to better understand the mechanisms of the impregnation of ILs inside the ionomer contained in the catalyst layer, SAXS studies were performed.

It was shown by EDX/ICP-OES that the immersion of the fuel cell electrodes in mild conditions can extract the Pt from the catalyst layer, depending on the IL. Indeed some ILs interact with the ionomer leading to a swelling of the ionic domains and plasticizing the polymeric aggregates. SAXS results (Figure 4B) illustrate the difference of behaviour between two different ILs. On the one hand, no difference was observed between Nafion membrane immersed in IL(A) and a dry Nafion membrane: the IL is not retained inside the ionomer. On the other hand, for IL(B) a leftward ionomer peak's shifting was observed: IL(B) incorporate and swell the ionic domains of the ionomer which reduce the cohesion inside the catalyst layer and in turn ends up to the Pt-NPs extraction. After this step, Pt-NPs were found stable in the selected ILs and detached from their carbon support (Figure 4C). Mechanisms of Pt-NPs extraction are currently discussed in the light of the SAXS results in a wider angular range.

This work is a part of a transversal thesis between INAC/LITEN/LETI and C2P2 laboratories (Mathias COUDRAY).

♠ **Platinum nanoparticles recycling from fuel cells with ionic liquids.** M. Coudray, E. Billy, H. Mendil-Jakani, P.-H. Haumesser, C. Santini, V. Dufaud*, Recycle & Reuse, 24-26 October 2018, Istanbul. Oral.*

Organic thin films for energy conversion technologies

Coll. INAC/SyMMES, LITEN

Organic semiconducting materials, and in particular pi-conjugated polymers, are nowadays widely employed in the field of organic (opto)-electronics. With the rise of organic photovoltaic performances (*L. Meng, et al., Science, 2018, eaat2612*) and the recent promising applications of organic materials for thermoelectric conversion (*D. Huang, et al., JACS, 2017, 139, 13013*), their potential for energy conversion technologies is incontestable. In particular, for thermoelectric conversion organic semiconducting materials show intrinsically low thermal conductivity ($\kappa \approx 0.1\text{-}1.0$ $W.m^{-1}.K^{-1}$) (*Y. Wang, et al., Macromolecules, 2017, 50, 857*) which is interesting for thermoelectric devices operating at low temperature (<200°C). However, the electrical conductivity, which is linearly related to thermoelectric performances, significantly varies from one material to another and is strongly influenced by the morphology or crystallinity of the sample. Thus, being able to correlate mobility and bulk morphology is a strong asset to design more efficient organic materials.

X-ray diffraction is performed on thin films to allow us to identify the preferential orientation and the presence of π-stacking interactions between polymer chains. Figure 5 exhibits examples of

diffractograms obtained on three different copolymers synthesized at SyMMES. The polymer P(FBDOPV-2T-C_{12}), in red, shows intense out-of-plane peaks at small angles and defined in-plane peak above 20°, these are characteristic of edge-on packing chains including π-stacking interactions. Interestingly, we can correlate this high degree of order to significantly higher electron mobility (10^{-1} >> $10^{-5/6}$cm².V^{-1}.s^{-1}) measured in field effect transistor (OFET) compared to the other polymers (Figure 6).

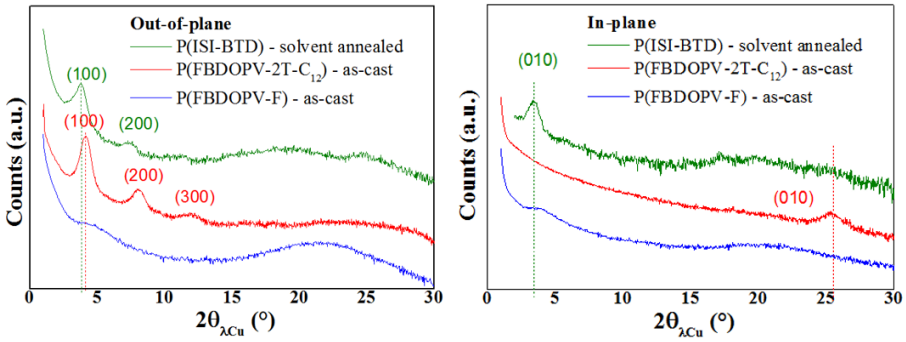

Figure 5 : Diffractograms of three polymer thin films. (Left), out-of-plane configuration. (Right), in-plane configuration.

In addition, we can determine the inter-lamella distances and, knowing the length of the lateral solubilizing alkyl chains, the inter-digitation percentage of those chains (figure 2). To conclude, XRD is a powerful tool to unravel the bulk morphology of polymer thin films and to understand the mobility and conductivity performances of these organic materials.

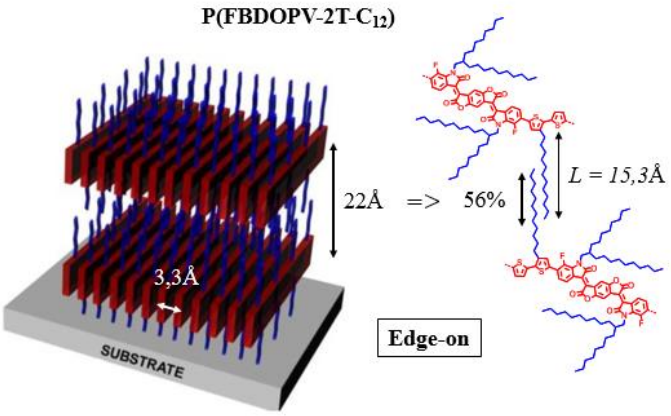

Figure 6: Schematic representation of P(FBDOPV-2T-C_{12}) thin film detailed morphology

Pillared graphene materials for enhanced energy storage

Coll. INAC/SyMMES/CAMPE

Electrochemical double-layer capacitors (EDLC), also known as supercapacitors (SCs), are devices that store energy through charge separation from electrolytic ion sorption on charged electrode surfaces. Porous carbons such as activated carbons (ACs) are traditionally used as electrode materials due to their high surface areas and low costs. In parallel to ACs, various graphene derivatives were proposed as potential materials for SCs owing to their high electrical conductivities, large surface areas and mechanical flexibilities. Reduced graphene oxide (RGO), readily prepared from graphene oxide (GO), is extensively studied as a model graphene-like material. RGO displays good power capability but suffers from low capacitances as the reduced graphene sheets partially restack through π- π interactions.

Exploring the layered structures of graphene derivatives for ion sorption is one of the approach followed in the group to avoid graphene layers restacking. The graphitic stack with 3.3 Å inter-layer separation is too small for ion sorption but could be tuned with an intercalant – also called pillared - to exhibit an expanded graphene layer structure. This methodology is also appealing to trigger the matching between electrolyte ion diameter and 2D porosity size (*ie.* graphene galleries height) that is known to promote the achievement of high capacitances.

Precedent results obtained in the group showed that pillared graphene materials with varied inter-layer separation using alkyl diamines (5, 6, 8, 10 and 12 Cs) as pillars could be readily obtained. XRD revealed the increase of graphene galleries height (d-spacing) with increasing pillar size (Figure 7a). Electrochemical tests performed in various electrolytes from the tetraalkylammonium (tetraethyl, propyl, butyl and hexyl – cations of increasing size) tetrafluoroborate (constant anion size) showed distinctly that cation with diameter above the d-spacing were not adsorbed inside these graphene galleries whereas those with a smaller diameter were (Figure 7b). This was the first example reported of ion-sieving inside graphene-based samples.

However, the capacitances obtained with these pillared graphene were not much higher than those recorded for reduced graphene oxide. Reducing the number of pillars was therefore attempted with the scope of increasing these values. XRD data showed that with reducing the number of pillars concentration, the d-spacing decreases slightly due to spacing out of the molecules or to a modification of molecules conformation (Figure 7c). The electrochemical tests performed showed greatly enhanced gravimetric capacitances (210 F/g – Figure 7d) explained by the improvement of ionic transport and the increase of adsorption active surface area in the graphene galleries not blocked by a high amount of molecules.

These pillared graphene materials were assembled into graphene hydrogel to optimize further the ions transport inside electrode bulk porosity. The impressive storage performances (Cv = 200 F/cm^3) achieved – among the best reported to date for graphene-derived samples - demonstrated the success of this strategy.

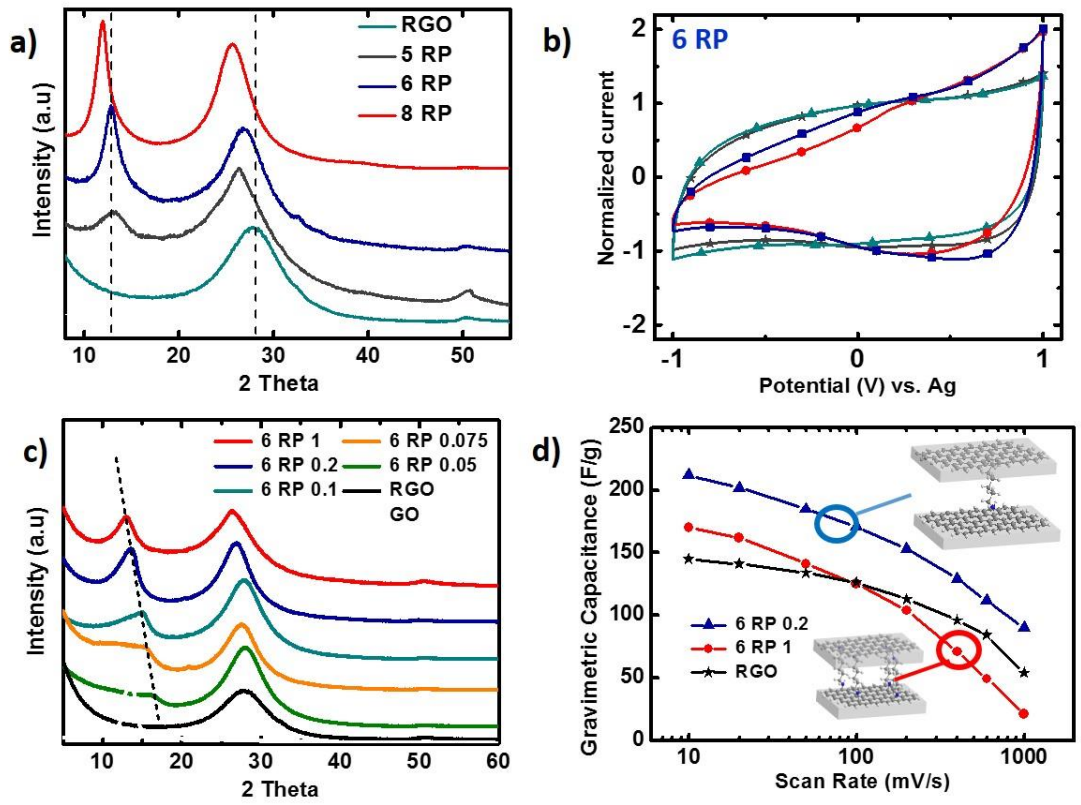

Figure 7: (a) XRD diffractograms recorded on pillared graphene materials obtained with 5, 6 and 8 Cs pillar – called 5, 6 and 8-RP - and on RGO; (b) electrochemical behaviour of 6-RP with TEA BF_4, TPA BF_4, TBA BF_4 and THA BF_4 1M in ACN; (c) XRD diffractograms recorded on pillared graphene materials with 6 Cs pillar and obtained with different number of pillar equivalents – called 6-RP1, 0.2, 0.1, 0.075 and 0.05 -; (d) power capabilities tests on 6RP-1, 6RP-0.2 and RGO.

♠ **Ion Sieving Effects in Chemically Tuned Pillared Graphene Materials for Electrochemical Capacitors.** Banda, H., Daffos, B., Périé, S., Chenavier, Y., Dubois, L., Aradilla, D., Pouget, S., Simon, P., Crosnier, O., Taberna, P.-L., Duclairoir, F. *(2018) Chemistry of Materials, 30 (9), pp. 3040-3047. DOI: 10.1021/acs.chemmater.8b00759.*

♠ **One-step synthesis of highly reduced graphene hydrogels for high power supercapacitor applications**. Banda, H., Aradilla, D., Benayad, A., Chenavier, Y., Daffos, B., Dubois, L., Duclairoir, F. *(2017) Journal of Power Sources, 360, pp. 538-547.*

♠ **Investigation of ion transport in chemically tuned pillared graphene materials through electrochemical impedance analysis**. Banda, H., Périé, S., Daffos, B., Dubois, L., Crosnier, O., Simon, P., Taberna, P.-L., Duclairoir, F*, Electrochimica Acta, Accepted.*

3D graphene/Si nanoparticules composites for Li-ion batteries

Coll. INAC/SyMMES/CAMPE, INAC/SyMMES/STEP

The goal of the SiBaLi project is to increase the anode storage capacities of Li-ion batteries based on Si nanoparticles, as well as to improve their cyclability. The approach followed here is to work on the modification of the surface of these silicon nanoparticles as well as on the formulation of the electrodes.

The idea was to prepare composites based on nanoparticles of Si and graphene (rGO, graphene oxide hydrogels ...). The graphene derivatives have been tested in order to preserve the electronic contacts between active components and additives (such as binders), as well as to reduce / limit the formation of SEI. They were then mixed with nanoparticles (NPs) of silicon (Si) coated or not with a carbon shell (Si@C), in order to form Si / graphene composites that could be directly integrated into the electrode formulations, without adding conductive additive.

Thus, graphene conductive networks (or graphene hydrogels) have been prepared to maximize contact between Si or Si@C nanoparticles within the electrode formulations. Different reaction times and drying methods were tested to vary the developed surface and the density. The electrodes tested in half-cells Li-ion showed good electrochemical performances in capacity and stability: they reached capacities greater than 1500 mAh/g over several hundred cycles. The characterization of these composites by XRD made it possible to highlight differences in reaggregation between the graphene sheets, as a function of the presence or absence of the C layer on the Si nanoparticles (Figure 8b), which probably indicates a stronger interaction between graphene and C coated nanoparticles.

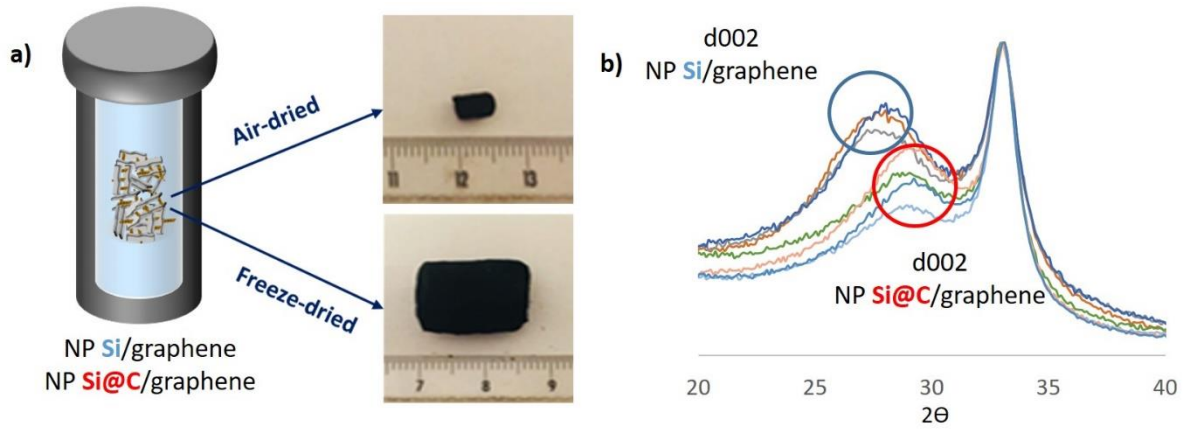

Figure 8 : (a) Pictures of the different materials obtained along with schematic representation of synthesis protocol ; (b) XRD diffractograms recorded for composites obtained with either Si nanoparticules or Si@C nanoparticules under different reaction time conditions and drying methods.

Study of the microporosity of hard carbons for sodium-ion batteries: relationship between the structure and the electrochemical performances of hard carbon derived from biomass

Coll. LITEN/DEHT/STB/LM

Today, lithium-ion batteries are used in a wide range of applications such as computers and mobile phones, and electric (EV) and hybrid (HEV) vehicles. However, the cost and accessibility of lithium resources could become a hindrance to the development of these batteries in the future. In this context, sodium-ion batteries are an interesting alternative. Hard carbon is among the most promising candidates for negative electrode materials even if its cycle capacity needs to be improved. The role of various factors such as the microstructure of hard carbons and the various mechanisms of sodium ion insertion is still the subject of debate to establish a link between the microstructure and the electrochemical performances.

The research on hard carbon anode material also needs of a low cost and high quality precursor. Today, hard carbon is mainly made of phenolic resins, which leads to a material two times more expensive than graphite. That is why, many studies are seeking for the viability of using biomass based hard carbon. The advantage of this source is its renewable nature, its low cost and its promising quality as precursor given its carbon content and C/O ratio. However, there is not a systematic study regarding biomass variability. More research needs to be done in order to understand the influence of the properties of the biomass precursor in the electrochemical performance of the hard carbon anode.

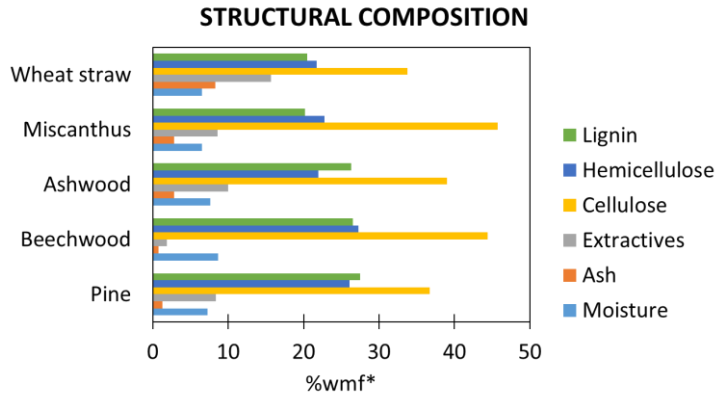

Figure 9. Main composition of biomasses used in this study.

The present study aims to correlate the microstructure of the final hard carbon with the properties of the raw biomass. For doing this, the hard carbons were obtained by pyrolysis of 5 biomasses species representative of France: Pine (resinous wood), Beechwood and Ashwood (decisious wood), Miscanthus (grass and energetic crop) and Wheat straw (cereal agricultural residue),

the main composition of these species are presented in figure 9. Three different temperatures were used for the synthesis: 1000 °C, 1200 °C and 1400 °C. Final samples were characterized by several techniques, but here we are going to focus on the *powder X-ray diffraction (XRD)*, and the *Small-Angle X-Ray scattering (SAXS).*

The XRD pattern (Figure 10) give an observation of the graphene plane organization as a function of the pyrolysis temperature. BM pattern corresponds to raw biomass in which crystalline cellulose is identified. After a first pyrolysis up to 450°C, there is a degradation of the crystalline cellulose and the other biopolymers (hemicellulose and lignin) leading to macroporous aromatic amorphous structure. This first structure tends to organize at higher pyrolysis temperatures, by forming aromatic clusters, the space between these clusters is consider as the internal porosity. However, given the high level of cross-linking in the initial polymeric precursor, it does not reach a perfect graphite lattice even at higher temperatures than 1400°C. Concerning different biomasses, the pattern is very different between the Pine and the Wheat Straw. Pine presents the typical hard carbon pattern and does not contain mineral picks at 1400 °C. Wheat Straw, has an important quantity of minerals in the carbon structure, even at 1400°C, mainly identified as moissanite (SiC), and the peaks corresponding to the hard carbon structure are widely modified. Raw biomass contain minerals within its carbonaceous structure recovered during its metabolic function and are concentrated during pyrolysis. These minerals are gathered as ashes in figure 10.

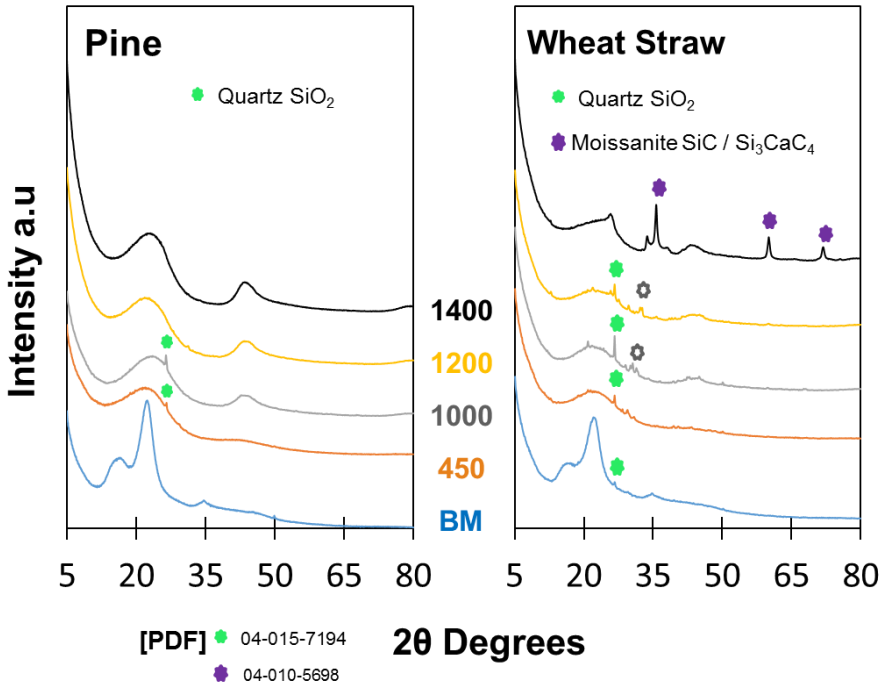

Figure 10. DRX Pattern of Pine and Wheat straw at different temperatures.

The SAXS laboratory measurements were used to characterize microporosity in the hard carbon samples (see Figure 11). The measurements showed a clear difference in the microstructure between the Ashwood and the Wheat Straw. Wheat Straw does not present a Guinier domain characteristic of well-defined internal porosity, maybe because of the high mineral content. However, Wheat Straw seems to exhibit higher superficial area. Notice also that there is an increase in size and in the number of micropores with the pyrolysis temperature that can be clearly observe for all woody biomasses, here represented by Ashwood. The best electrochemical performances are obtained for woody biomasses at the highest temperature.

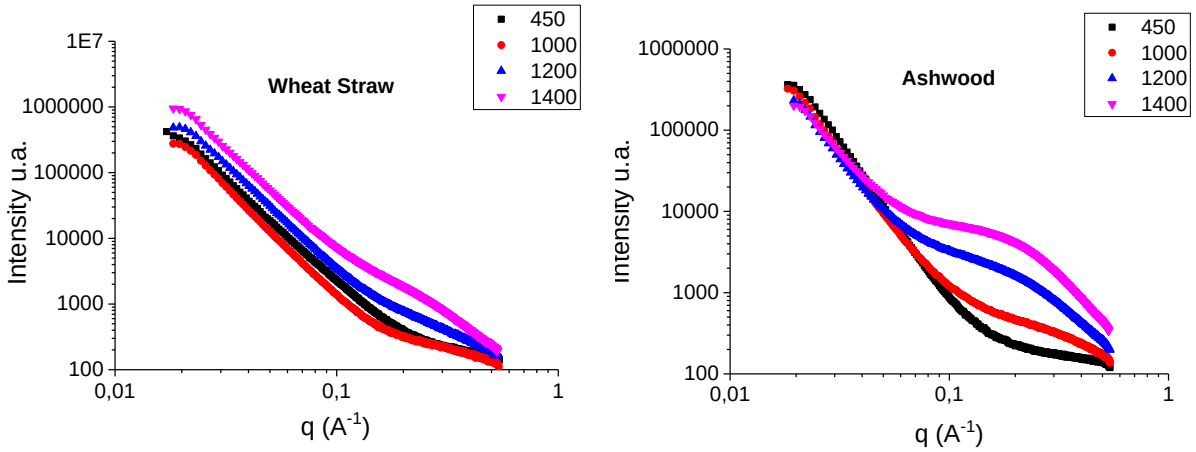

Figure 11. SAXS spectra for Wheat Straw and Ashwood at different temperatures

.

In conclusion, this first experimental approach suggests that biomasses with a lesser content of initial ashes tend to develop a well define internal microporosity that enhances the insertion of sodium ions. While a high content of initial ashes does not seem beneficial for sodium insertion in the carbonaceous matrix, but could lead to alternative applications to this kind of structure containing SiC. Research is still on the go to evaluate in details all other biomasses properties.

♠ **Biochars from various biomass types as precursors for hard carbon anodes in sodium-ion batteries.** C. Saavedra Rios, V. Simone, L. Simonin, S. Martinet, C. Dupont. *J. Biomass and Bioenergy* ***117*** *(2018) 32–37*

Si-based anodes for lithium-ion batteries

Coll. INAC/SyMMES, IRAMIS/NIMBE

Lithium-based batteries are already the energy storage for small and medium devices. However, there are still necessary materials that can insert high quantity of lithium ions. In the search for materials with these characteristics, silicon offers interesting possibilities because of its high capacity (3579 mAh/g) and natural abundance as compared with the commercial electrode, graphite (372 mAh/g). Nevertheless, silicon suffers large volume expansion upon the insertion-disinsertion of the lithium ions, which allows the continuous formation of Solid Electrolyte Interface (SEI), leading to Li trapping and capacity loss. This continuously happens, leading to irreversible capacity and electrical contact loss. One way of limiting volume expansion is using silicon nanoparticles, where the small size enables Li transportation and strain relaxation. The nanoparticles can also be embedded in a matrix, thus forming a composite material. This type of material displays better behavior with respect to the aging effect: less capacity loss due to reduced SEI formation. Another possible solution is the insertion of a different element in the silicon structure. Germanium, for instance, can improve the electronic and ionic conductivity, allowing better lithium diffusion and improving the performance.

SiGe alloys for lithium-ion batteries

Si_xGe_{1-x} alloys have shown to improve the performance during cycling compared with Si-rich electrodes. In the frame of a collaboration with CEA Paris Saclay/IRAMIS/NIMBE, 3 different $Si_xGe_{(1-x)}$ nanoparticles (NPS) alloys were synthesized: $Si_{0.3}Ge_{0.7}$, $Si_{0.7}Ge_{0.3}$, and $Si_{0.44}Ge_{0.55}$ by laser pyrolysis. This technique consists in using a laser beam for decomposing silane and/or germane to obtain the NPs in the range of 20 – 100 nm (see Figure 12a). For the three compounds, the $\theta/2\theta$ X-ray diffraction data displays diffraction peaks characteristic of the expected diamond structure but the peak shapes indicate the presence of inhomogeneities in $Si_xGe_{(1-x)}$ composition.

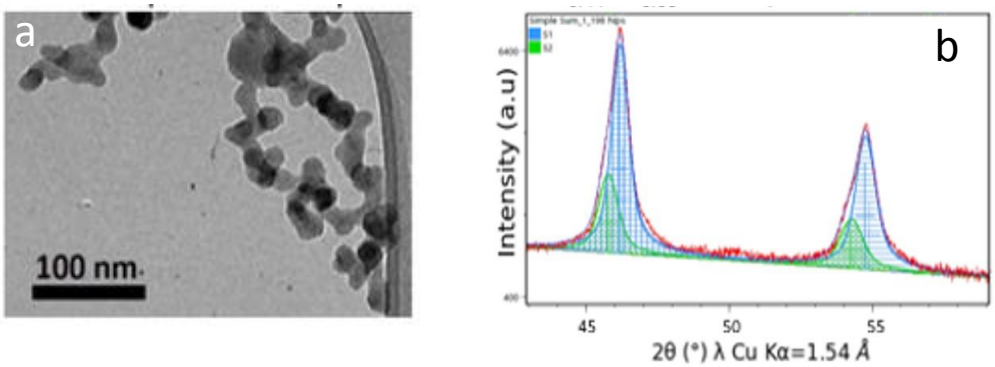

Figure 12: (a) STEM picture of Si Nps ; (b) $\theta/2\theta$ X-ray diffraction of $Si_{0,44}Ge_{0,55}$ NPs and LeBail profile refinement

Data was analyzed by LeBail profile refinement, assuming the presence of diamond type crystalline phases with different lattice parameters to account for the chemical composition dispersity. In the case of the $Si_{0.44}Ge_{0.56}$ compound, two different phases were considered (see Figure 12b). The fitted values of the lattice parameter corresponds to silicon contents x=0.23 and x=0.44. Considering the differences in peak integrated intensities corrected from the different electronic densities, the relative amounts of the two crystalline phases (x=0.23 and x=0.44) are of the order of 1:3. The germanium rich $Si_{0.3}Ge_{0.7}$ compound reveals polydispersity. Four different phases were needed to account for the peak shape. The Si content values deduced from the refined lattice parameters range from x=0.0 (pure Ge) to x=0.3. The $Si_{0.7}Ge_{0.3}$ compound appeared to be more homogeneous. Two phases had to be considered with equivalent amounts, giving a mean Si content <x> = 0.55. Considering the relative intensities of background and diffraction peaks, $Si_{0.7}Ge_{0.3}$ shows less crystallinity than the two other compounds.

The SiGe alloys were used to prepare negative electrodes for operando synchrotron combined SAXS/WAXS experiments, with the aim of probing the nanoparticles nano- and atomic scale structure along the electrochemical cycling. The data analysis is in progress.

Delithiation kinetics in an industrial composite for lithium-ion batteries

Our aim is to understand the lithiation mechanism in a complex industrial composite graphite/ amorphous Si + $FeSi_2$ (identified as Sintbat in the following), and compare its behaviour to the one of pure graphite on the one hand and also of a model composite made of crystalline Si Nps and graphite on the other hand. Coin cells were prepared using the three different compounds. Subsequently, it was performed one complete cycle and one lithiation between 1 V – 10 mV (see Figure 13a). The cells were then opened in the glovebox and the X-ray diffraction samples were prepared using the sample holder shown in Figure 13b sealed with two Kapton foils.

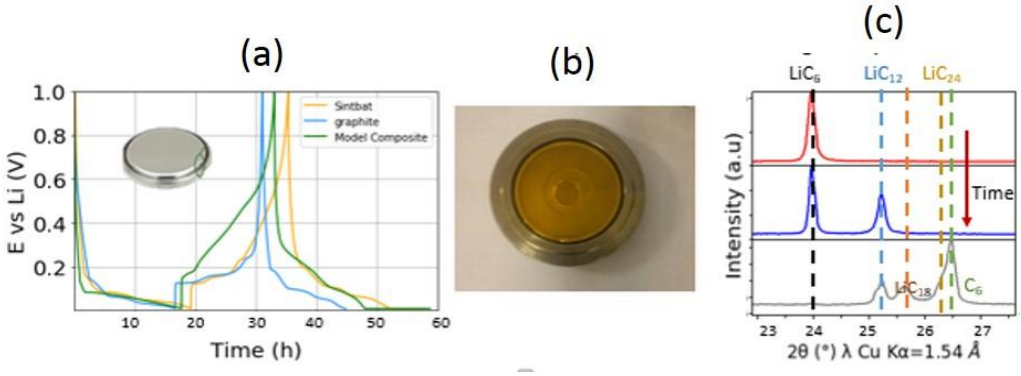

Figure 13 – (a) Cycling electrochemical data – (b) Sample holder used for XRD measurements – (c) Evolution of the LiCx diffraction peaks along the graphite delithiation process.

The measurements were made using the Panalytical X'pert diffractometer. Scattering angles 22 – 30° were collected in 0.02° steps with count time of 40 s per step to follow the kinetics of the LiC_x phases'

formation until the graphite peak appears at 26.5° (see Figure 13c). Figure 14 displays the delithiation kinetics determined from the evolution of the area of the LiC_6 and LiC_{12} (002) diffraction peaks, for the three types of electrodes. Clearly the pure graphite delithiation is much slower than the one observed in the presence of silicon. Nevertheless, the spontaneous pure graphite delithiation indicates that the cell is not sufficiently airtight. So we decided to suspend this study pending a new better-adapted cell, which should be available early 2019.

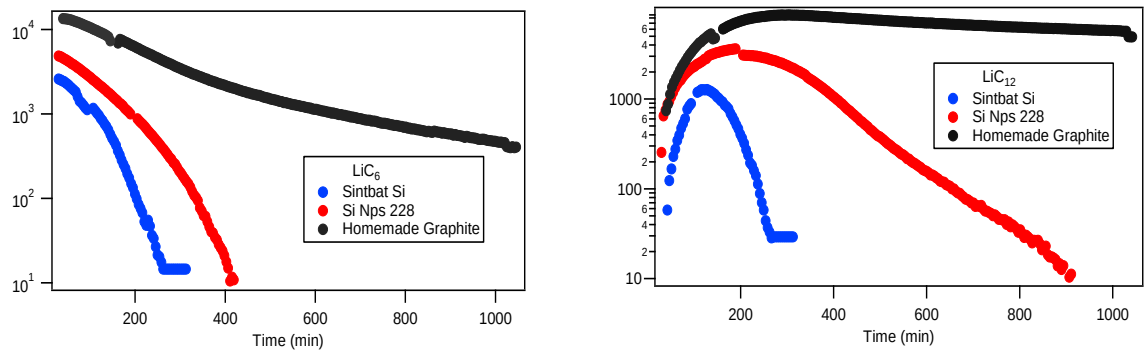

Figure 14- Graphite delithiation kinetics: evolution of the LiC_6 and LiC_{12} (002) diffraction peaks areas as a function of time (t=0 corresponds to the exit of the cell out of the glove box.)

Hybride perovskite for photovoltaic applications

Coll. INAC/SyMMES, LITEN/LMPO

These past few years, hybrid halide perovskites appeared as a promising active material for solar cells. Efforts made by research groups all over the world allowed to reach record solar cells efficiencies of 23 % in less than a decade. Such performances are due to the outstanding properties of the hybrid halide perovskite material: electron-hole diffusion length reaching 1 µm, low exciton binding energies, high absorption coefficient, tunable bandgap... Despite great technological advances, fundamental understanding of the material is still lacking. Crystallization mechanisms, I-V hysteresis in the solar cell devices phenomenon, stability issues… all these questions are still under intensive study. $CH_3NH_3PbI_3$ (MAPI) can be considered as the reference hybride perovskite material. It crystallizes in a tetragonal structure at room temperature, with PbI_6 octehadrons forming a 3D network. 8 corner sharing PbI_6 octahedrons creates a cage which center is occupied by the organic cation MA^+. MAPI undergoes a first order tetragonal <-> cubic phase transition around 60°C. Previous studies have shown that using a chlorine precursor ($PbCl_2$ instead of PbI_2) leads to thin layers with enhanced properties. Due to the differences in the ionic radii of I and Cl, the chlorine atoms are not incorporated in the perovskite structure, however, textured MAPI thin layers (Figure 15), with larger grain sizes and ten times higher charge carrier diffusion length are obtained when using chlorine in the inital growth conditions.

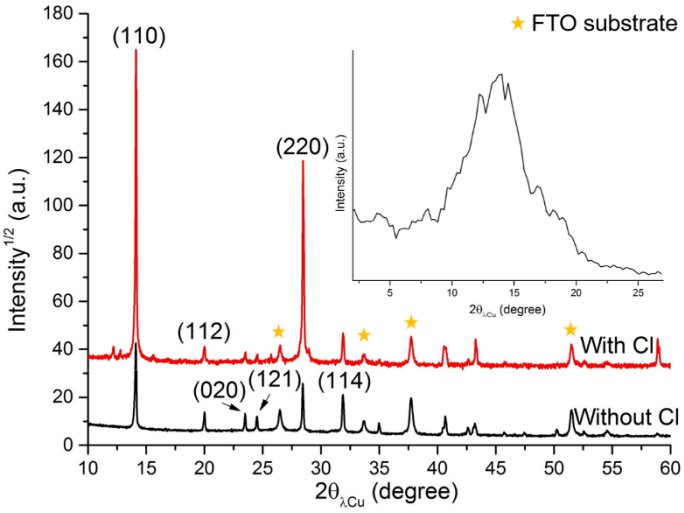

Figure 15: XRD patterns of MAPI thin layers deposited on FTO/TiO2 substrate. The black curve corresponds to the sample made without Cl in precursor solution and the red curve is with Cl. The insert show the rocking measured at the (220) diffraction peak of MAPI when using chlorinated precursor.

In the frame of the collaboration between SGX and SyMMES at INAC and LMPO at INES, a study was conducted on the crystallization mechanisms of MAPI thin layers.

Understanding the formation reaction of hybrid perovskites is essential to optimize process and fabrication conditions as well as to achieve better optoelectronic properties. Our precursor solution is a mixture of MAI (methylammonium iodide) and $PbCl_2$ (ratio 3: 1) in DMF (dimethylformamide). This solution is deposited by spin coating in a single step. This solution is not miscible, hence the need to filter it before deposition.

Crystallisation mechanisms

In order to determine the intermediate phase formed before the formation of the MAPI, we characterized the film obtained after depositing the solution of precursors and without annealing. XRD results show the presence of a highly oriented crystalline cubic phase. According to the literature, it should be the chlorinated perovskite $MAPbCl_3$, (Space Group Pm-3m, a=5.67 Å). We performed XRD

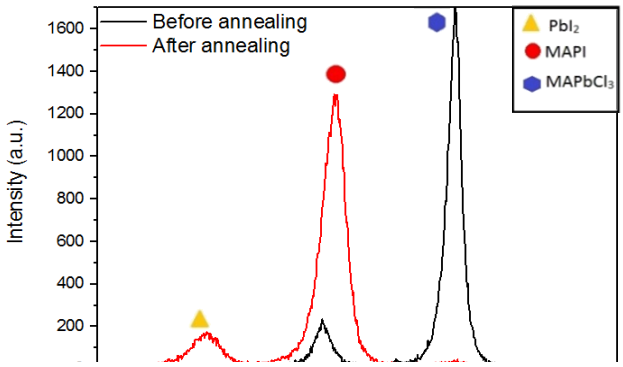

Figure 16. XRD characterization of the MAPI layer before annealing (in black) and after annealing (in red)

measurements (cf. Figure 16) on the SmartLab diffractometer during in situ annealing of the sample at 100°C, under a nitrogen flow. These results reveal the formation of the MAPI from this chlorinated perovskite the amount of which decreases as the annealing progresses.

Different publications report the formation of chlorine based lamellar reaction intermediates. In order to confirm the presence of the MAPbCl3 phase, we carried out in plane measurements on the SmartLab diffractometer, on a sample where chlorinated perovskite remains present after annealing. These in plane measurements clearly show the presence of the $MAPbCl_3$ cubic phase Bragg peaks (cf Figure 17).

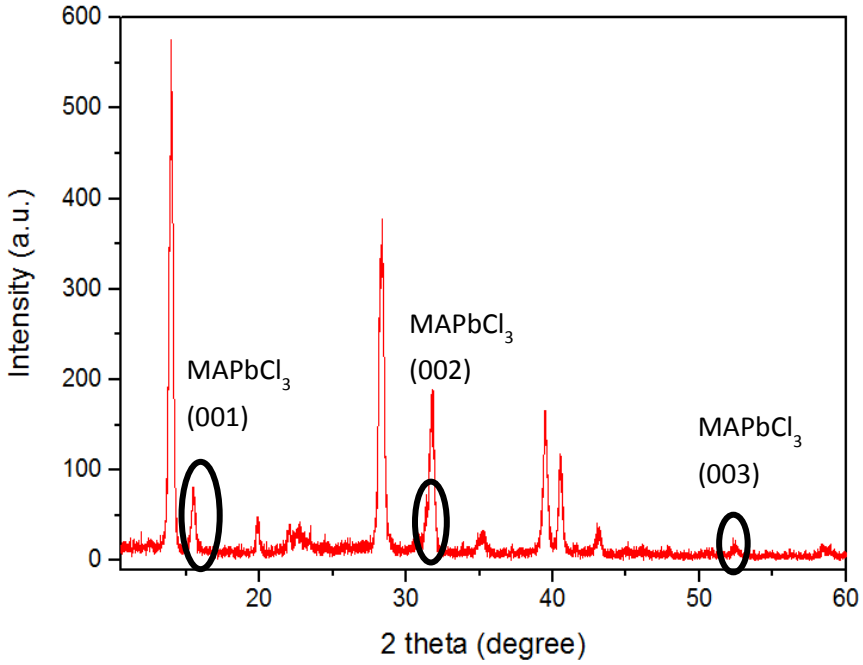

Figure 17. In plane measurements (ω=0.35°) showing the presence of $MAPbCl_3$ cubic phase

Double texture

As mentioned earlier, the thin layers obtained from chlorinated precursors are mainly textured along the (hh0) MAPI direction. However, the (hh0) peaks often appear to be splitted (Figure 18a). Two hypothesis were proposed to explain the phenomenon:

- a cubic / tetragonal phases coexistence in the thin layers (already observed in MAPI powders and single crystals),
- a double texture [hh0]/[00l] of the thin layers due to twinning.

A Reciprocal Space Map (RSM) was performed on the Panalytical Empyrean thin film diffractometer (Figure 18b). The sample studied was a MAPI thin layer deposited on a single-crystalline TiO_2 substrate, exhibiting the peak splitting. The combination of $\theta/2\theta$ scan and RSM proved, via lattice parameters

calculations, that the two populations both correspond to the tetragonal phase. Temperature dependent XRD measurements performed on the Panalytical X'Pert diffractometer on samples presenting the two peaks confirmed the formation of twins when passing from the cubic to the tetragonal phase, and a temperature dependence of the cell volume in agreement with the litterature.

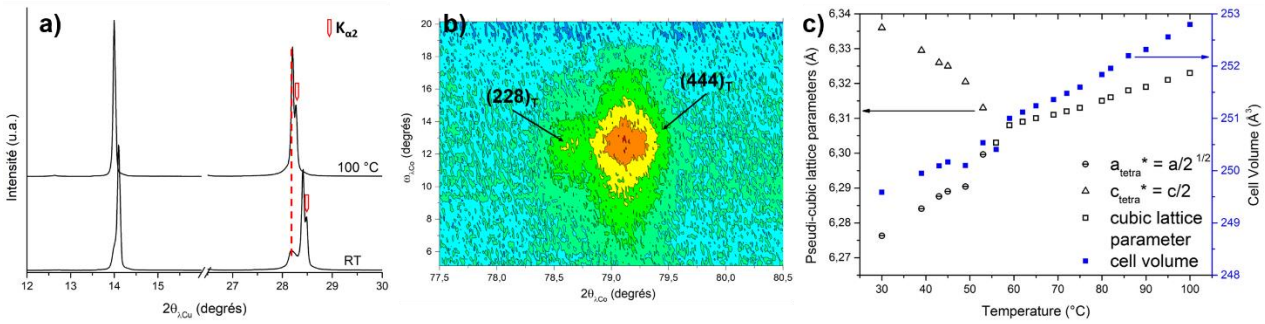

Figure 18 (a) ϑ-2ϑ diffractogram of a sample exhibiting a splitting of the (hh0) peaks in the tetragonal phase. (b) RSM measured on a sample exhibiting the double peaks, giving access to in plane lattice parameters. (c) Evolution of the lattice parameters and volume upon heating, confirming the hypothesis of a double texture.

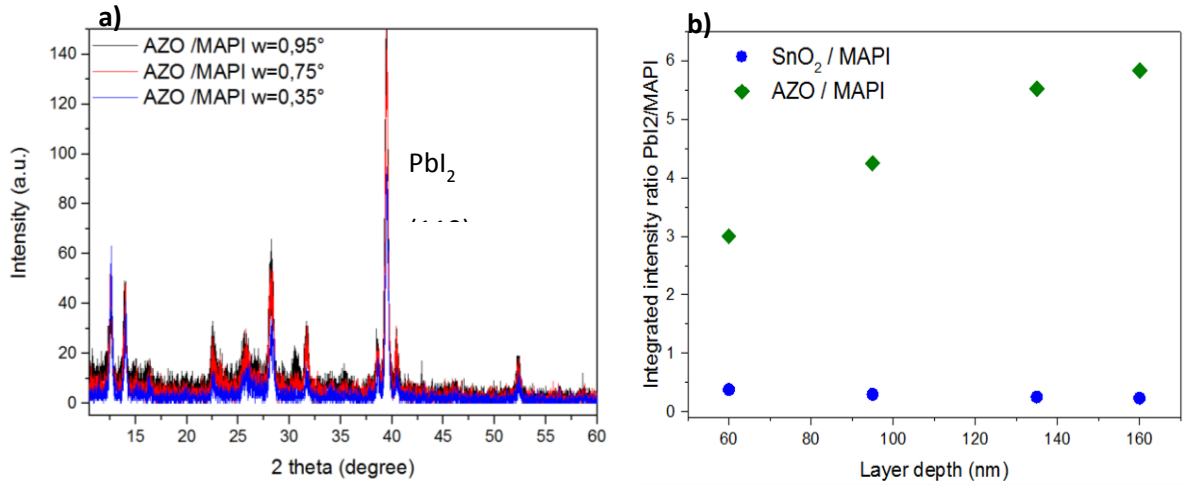

Figure 19. (a) In plane measurements showing the variance of peak intensity of PbI_2 with the angle incidence (ω=0.35°, 0.75° and 0.95°) for AZO / MAPI layers, (b) Integrated intensity ratio of PbI_2/MAPI in function of layer depth for both SnO_2/MAPI and AZO/MAPI layers

MAPI film ageing

Another part of the study consisted in the characterization of aged perovskite layers in order to determine the degradation routes. We carried out in plane measurements with aged perovskite layers in order to determine the localization of PbI_2, the main degradation product. Varying the incident angle

allows to probe the layer for different penetration depths. Our measurements revealed that the distribution of PbI_2 formed by the degradation depends on the nature of the N layer (layer under the perovskite). For AZO /MAPI layers, PbI_2 is distributed more in depth, therefore at the interface with AZO layer. On the other hand, for SnO_2/MAPI layers PbI2 appears to form from the surface (cf. Figure 19)

♠ **Activation Energy of Organic Cation Rotation in CH3NH3PbI3 and CD3NH3PbI3: Quasi-Elastic Neutron Scattering Measurements and First-Principles Analysis Including Nuclear Quantum Effects**. Li J., Bouchard M., Reiss P., Aldakov D., Pouget S., Demadrille R., Aumaitre C., Frick B., Djurado D., Rossi M., Rinke P., *J Phys Chem Lett. 2018 Jul 19;9(14):3969-3977*

♠ **Direct Evidence of Chlorine-Induced Preferential Crystalline Orientation in Methylammonium Lead Iodide Perovskites Grown on TiO_2**, Bouchard M., Hilhorst J., Pouget S., Alam F., Mendez M., Djurado D., Aldakov D., Schülli T., Reiss P*., J. Phys. Chem. C 2017, 121, 7596-7602.*

Doping and surface effects of $CuFeS_2$ nanocrystals used in thermoelectric nanocomposites

Coll. INAC/SyMMES

Among energy harvesting devices, thermoelectric generators able to harvest heat from ubiquitous temperature gradients are of special interest due to their long-lasting continuous operation without maintenance, absence of vibration or noise, and small size. Being compatible with extreme temperatures, they are used in space applications since the 1950s. However, they rarely gained wide market applications because of their low energy conversion yields. Today, the advent of new, low power electronic devices opens new niche markets for small and robust electrical power generators. In particular, devices running on the Internet of Things often require low power, and demand unsupervised long-lasting operation in a large variety of locations and situations. Among potential materials there is an increasing interest for the development of environmentally friendly and safe thermoelectric compounds. We focus here on chalcopyrite ($CuFeS_2$) nanocrystals. Cu, Fe and S are earth abundant and non-toxic elements and chalcopyrite can be produced in large quantity in form of nanoparticles by top-down approaches from the natural mineral (an abundant ore) or by bottom-up methods via colloidal synthesis. $CuFeS_2$ exhibits an appropriate band gap (0.6 eV) for use in thermoelectrics and is available both in the n-type and p-type doped states, with a relatively high electrical conductivity of around 500 S/m. However, its elevated thermal conductivity of 7.8 $W/m{\cdot}K$ has to be decreased to enable its use in thermoelectric energy conversion, e.g. by tuning its nanostructure.

In this work we present a novel method optimized for synthesizing $CuFeS_2$ nanocrystals (NCs) of controlled stoichiometry and with a mean size of 40 nm. This size range is difficult to achieve as steric stabilization in organic solvents is generally limited to particle sizes below 20 nm. Powder X-ray diffraction (Figure 20) reveals the presence of a wurtzite majority phase (space group $P6_3mc$), which

coexists with a tetragonal chalcopyrite minority phase (space group I-42d). Although unobserved in the bulk, the wurtzite phase of $CuFeS_2$ has already been reported once before for nanoparticles. For the evaluation of their thermoelectric properties, the $CuFeS_2$ NCs were first annealed under vacuum at 400 °C for 1 hour to remove the organic capping layer, and then hot-pressed (400 °C, 0.5 t) into 8 mm disc-shaped pellets. The pellet density of 3.6±0.2 g/cm^3 (bulk chalcopyrite density 4.19 g/cm^3) corresponds to a compactness of 85±6%. As seen by SEM, the pellets are composed of slightly larger faceted NCs of around 60 nm, indicating sintering during the hot-pressing. The X-ray diffractogram displayed in Figure 21 shows a diffraction pattern characteristic of the chalcopyrite $CuFeS_2$ phase with no indication of the presence of the wurtzite phase. A Rietveld refinement of the data based on the chalcopyrite structure was performed, giving the following values for the lattice parameters: a = 5.290(2) Å, c =10.426(4) Å. The refinement of the site occupancies is in agreement with the expected stoichiometry. The refined crystallite size (60±10 nm) is significantly larger than for the pristine NCs (30 ±10 nm). The heat treatment thus resulted in a wurtzite-to-chalcopyrite phase transition, accompanied by the coalescence of the pristine crystallites to larger ones.

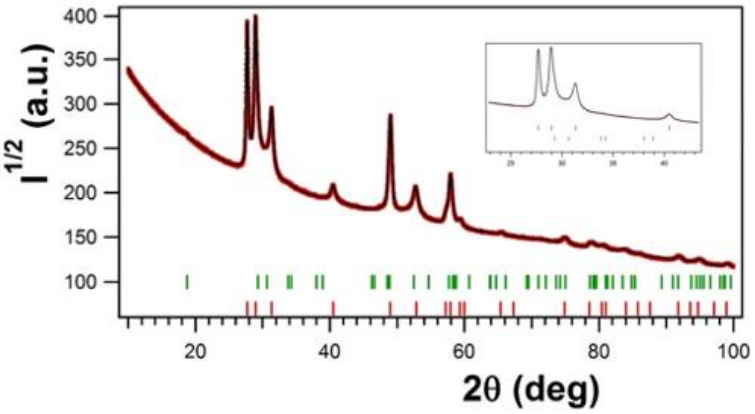

Figure 20: Powder X-ray diffractogramm obtained with the pristine NCs (red: experimental data – black: calculated pattern from individual peak refinement – the vertical lines indicate the expected peak positions for the hexagonal (red) and tetragonal (green) CuFeS2 crystalline phases). Inset: zoom evidencing the coexistence of the two phases.

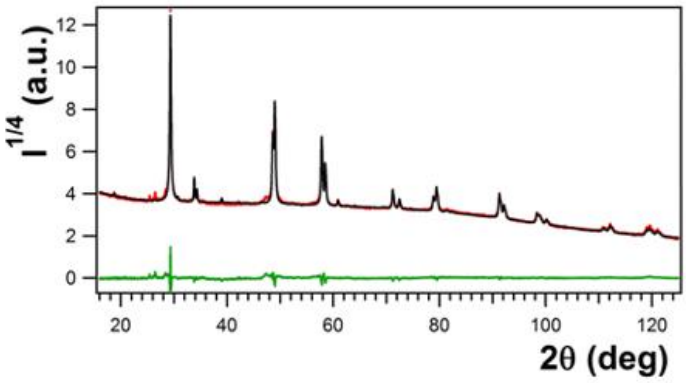

Figure 21: X-ray diffractogram obtained with crushed hot-pressed pellets (red: experimental data – black: calculated pattern from Rietveld refinement based on the pyrochlore crystalline phase – green: difference plot).

♠ **Doping and Surface Effects of CuFeS2 Nanocrystals used in Thermoelectric Nanocomposites**, L. Vaure, L. Yu, F. Agnese, D. Aldakov, S. Pouget, A. Cabot, P. Reiss, P. Chenevier, *2018, ChemNanoMAt 4(9), 982-991*

GISAXS investigation of (functional) block copolymer (BCP) thin films

Coll. INAC/SyMMES

Hierarchically self-assembled functional A-*b*-B block copolymers for solving next generation (electrochemical) energy storage issues precisely encode *tuneable by design* ionic transport function with mechanical property via ionically conducting (A) sub-block covalently linked to an insulating conducting (B) sub-block. Thanks to the new GISAXS configuration recently implemented onto the SAXS instrument at INAC, the self-organization of different functional BCP thin films have been recently characterized to get proof of concept demonstration of its performances. Obtaining long-range ordered nanostructures from (functional) thin films BCPs deposited onto flat substrates was challenged by different annealing processes. Model systems from different international research collaboration projects were investigated by researchers of UMR5819-SyMMES (CEA/CNRS/UGA) and INAC/MEM/SGX. Two examples are described hereinafter.

A biosourced High χ-Low N BCP consisting in a model $PS_{3.8k}$-*b*-$MH_{1.2k}$ system forming flat-lying cylinders ordered thin films upon annealing conditions was first studied. This film was previously characterized at ESRF (onto BM02-D2AM beamline: see Fig. 22b) under the same annealing conditions (microwave + solvent annealing) to be benchmarked with the capabilities of the new INAC GISAXS setup (Fig. 22a). The BCP thin film consists on a thin (100 nm thick) copolymer film flat lying onto a Si/SiO_2 substrate. The comparison of the two GISAXS 2D patterns clearly validates the performances of the GI-SAXS configuration at INAC laboratory to allow for the surface structuration/ordering of (functional) block copolymer thin films.

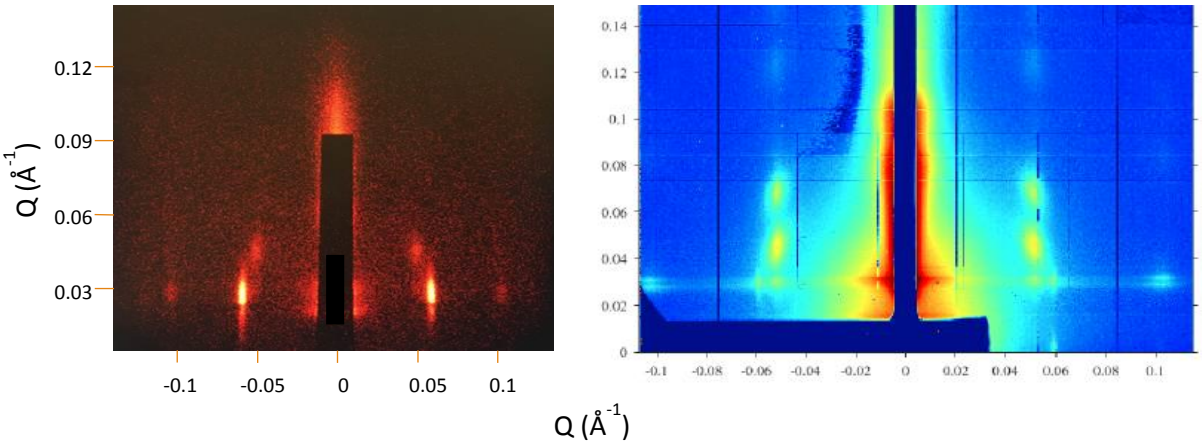

Figure 22: (a) 2D GI-SAXS pattern acquired @ INAC with a sample/detector distance of 180 cm. (b) 2D GI-SAXS pattern acquired @ ESRF/BM02-D2AM) with a sample/detector distance of 188 cm.

The second functional thin film BCP tested @ INAC was an as-cast PS_{26k}-*b*-$P2VP_{26k}$ BCP thin film further subjected i) to a first solvent annealing procedure and then ii) to a vapour phase post-chemical modification with methyl iodide (MeI) in order obtain ionically conducting PS_{26k}-*b*-$MeP2VP_{26k}^{+}/I^{-}$ thin film laying onto PS-*r*-P2VP-OH brushes (PS 48 wt.%). Comparison of Fig.23a vs 23b clearly show features of the long-range ordering induced by the solvent annealing while Fig.23b vs 23c manifest the positive impact of the selection of the P2VP sub-block with MeI in leading to a long range ordered block copolymer electrolytes of great scope for electrochemical energy storage devices

Figure 23: *2D GI-SAXS patterns from* (a) *as-cast BCP thin film* (b) *a solvent annealed BCP thin film. (c) a solvent annealed chemically modified (with MeI) BCP thin film.*

The targeted next evolution of the GISAXS setup @ INAC will be the implementation of a temperature controlled plate complementing the recently developed home-made multimodal platform (CNRS@SyMMES) coupling Polarized Optical Microscopy (POM), Electrochemical Impedance Spectroscopy (EIS) with or without application of an ac-electric field. This will allow *state of the art* in situ/operando multiscale multiphysic studies @ INAC onto functional thin film electrolytes for next generation electrolytes to trigger the dawn of 2.0 solutions *towards safer by design* higher performance solid-state energy devices required to implement the ecological transition process in response to the pressing societal issues consisting in ensuring access to affordable, reliable, sustainable & modern energy.

♠ **Alignment of Nanoplates in Lamellar Diblock Copolymer Domains and the Effect of Particle Volume Fraction on Phase Behavior**, N.M. Krook, J. Ford, M. Maréchal, P. Rannou, J. S. Meth, C.B. Murray, R.J. Composto, 2018, *ACS Macro Lett.* **7**, 1400-1407. DOI: 10.1021/acsmacrolett.8b00665– Cover picture December 2018

♠ **Alignment of Nanoplates in Lamellar Diblock Copolymer Domains and the Effect of Particle Volume Fraction on Phase Behavior**, C.B. Murray, N.M. Krook, M. Maréchal, P. Rannou, J.S. Meth, R.J. Composto, 2019, Spring ACS National Meeting, Orlando (Etats-Unis) - Invited oral communication

♠ Soft electrolytes with controlled organisations for energy storage and conversion, M. Maréchal, P. Rannou, 2019, 18th IUPAC International Symposium on Solubility Phenomena & Related Equilibrium Processes-ISSP18, 15-20/07/2018, Tours (France) - Invited oral communication

Environment / Catalysis / biological applications

Fe-based aziridination catalysts.

Coll. BIG/LCBM

Amines are essential compounds in biology, pharmacy and agriculture and their syntheses and modifications motivate a strong effort especially in pharmaceutical laboratories. Among them, aziridines attract special interest due to both their intrinsic properties and role as intermediates in numerous synthetic pathways. From the various methods proposed to access amines, nitrene transfer reactions have attracted strong interest because of their capacity to form amines directly without pre-functionalisation and postdeprotection. However, selective nitrene transfer reactions require catalysis by a metal species and the best catalysts developed so far are based on rare metals which are both expensive and toxic. Their replacement by more ecologically and economically friendly metals is intensively searched for with a strong emphasis being put on Fe catalysts. However their development is presently hampered by the limited mechanistic understanding of these reactions, many groups have taken iron oxygenases as an inspiring source.

In this context we develop an integrated experimental and theoretical approach to elucidate the mechanism of aziridination, a key reaction to access specific drugs among other compounds, so as to be able to conceive and optimize efficient catalysts. Structural characterization of catalysts precursors and optimally intermediate active species by X-ray diffraction techniques is both a preamble to catalysis studies by providing undisputable characterization and a validation of the correctness and precision of the theoretical calculations. Ultimately the efficiencies of various catalysts were shown to be coherent with the electron affinity calculated for the corresponding active species and in agreement with a mechanism involving a partial charge transfer in the transition state.

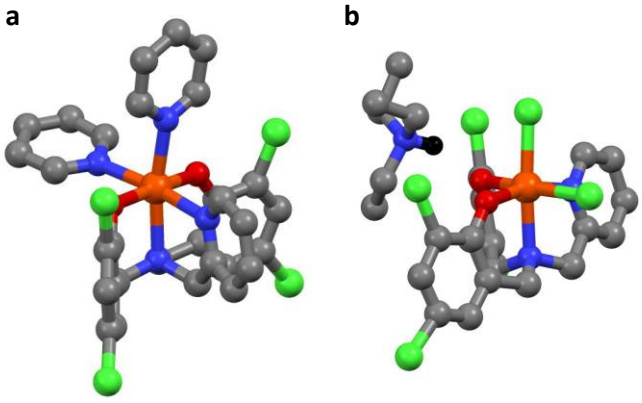

Figure 1: X-ray structures of (L^{Cl})Fe(II)$(Py)_2$ (a) and [(L^{Cl})Fe(III)Cl_2](NEt_3) (b)
Fe: orange, O red, N blue, Cl green, C grey, H black

♠ **Rational Design of Fe Catalyts for Olefin Aziridination through DFT-based Mechanistic Analysis.** R. Patra, G. Coin, L. Castro, P. Dubourdeaux, M. Clémancey, J. Pécaut, C. Lebrun, P. Maldivi, J.-M. Latour, *Catalysis Science and Technology* **2017**, *7*, 4388-4400.

H_2 evolution catalysts.

Coll. BIG/LCBM

The design of biomimetic catalysts for H_2 evolution has been the core expertise of the group since 2012 (in the BioCat team). We continued this approach in the last period with remarkable success in two directions:

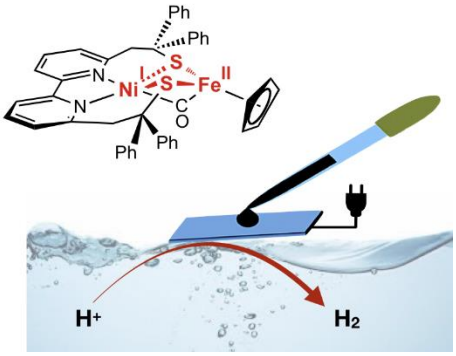

- First, in collaboration with the group of C. Duboc (Department of Molecular Chemistry, Grenoble), we developed novel NiFe catalysts reproducing key structural, spectroscopic and reactivity features of the active site of [NiFe] hydrogenases. We could namely isolate a Ni-Fe complex in three forms mimicking the Ni-SI (resting), Ni-L (reduced) and Ni-R (hydride-containing) states of the enzyme. This catalyst proved highly active for H_2 evolution under electro-assisted conditions in non-aqueous solvents (D. Brazzolotto et al.Nature Chemistry 2016, 8, 1054–1060). After chemisorption onto carbon electrodes, we could evidence H_2 evolution catalysis from aqueous solution through an enzyme-relevant mechanism triggered by the reduction of the species at the Ni(I)-Fe(II) state (ME. Ahmed Angew Chem 2018, 57,16001-16004);

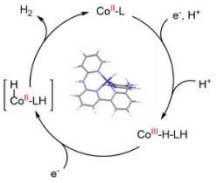

scheme of the catalytic cycle of a polypyridine cobalt complex

- Second, we designed polypyridine cobalt complexes with novel coordination spheres including redox-active ligands and proton relays. These complexes are soluble in water and display good activity for H_2 evolution *CO_2 reduction catalysts*. We applied bio-inspiration concepts to the design of a series of highly selective and active molecular catalysts for CO_2 conversion. Indeed the active sites of CODH and formate-dehydrogenase contain basic sites in the vicinity of the metal sites where CO2 is activated. We could demonstrate that the introduction of amine residues in the second coordination sphere of cyclopentadienyl cobalt diphosphine complexes completely modify the reactivity of the complexes towards CO_2, allowing them to selectively catalyze the formation of formate in DMF.

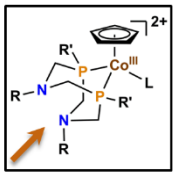

CO_2 reduction

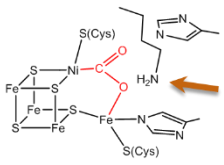

Active site of CODH

♠ **A noble metal-free photocatalytic system based on a novel cobalt tetrapyridyl catalyst for Hydrogen production in fully aqueous mediumsystem based on a novel cobalt tetrapyridyl catalyst**, N. Queyriaux, E. Giannoudis, C. Windle, S. Roy, J. Pécaut, A. G. Coutsolelos, V. Artero, M. Chavarot-Kerlidou, *Sustainable Energy & Fuels, 2018, 2, 553 - 557*

♠ **Molecular cobalt complexes with pendant amines for selective electrocatalytic reduction of carbon dioxide to formic acid**, S. Roy, B. Sharma, J. Pecaut, P. Simon, M. Fontecave, P. Tran, E. Derat, V. Artero., *J. Am. Chem. Soc. 2017, 139(10), 3685-3696*

Stabilizing highly reacting carben radicals

Coll. UGA/DCM

The discoveries of stable versions of elusive intermediates are historic landmarks, which have had deep impacts on modern organic chemistry, and beyond. Stable carbenes and radicals are typical examples. Although they were regarded essentially as academic curiosities when they were first disclosed, their uncommon properties have led in the long term to groundbreaking innovations in a remarkable range of scientific fields, including catalysis, material science and even medicine. We recently synthesized a handful of such organic patterns. At each step of the syntheses, X-ray crystallography of single crystals were key for assessing the identity and structure of the original novel functionalities

- We reported the isolation of a pyrimidinium-2-ylidene: a cationic carbene, which was hitherto believed to be too reactive to exist in standard conditions. The organometallic complexes are air-stable and are actually evaluated as original catalysts.

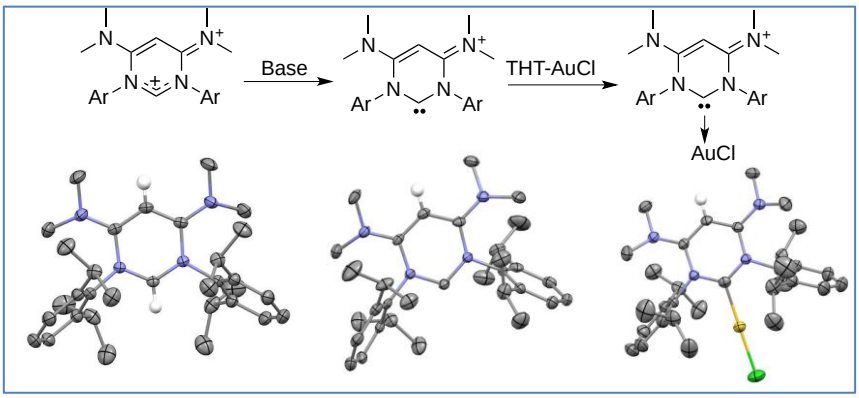

Figure 2: Localization of the cation and the radical obtained from the structure resolution.

- Introduction of an oxygen in C-5 position of these patterns led to biradicaloids, which were predicted as potential dyes for several applications, but considered as unreasonable organic compounds. Again, we showed they could be perfectly air-stable, despite non-canonical electronic structures.

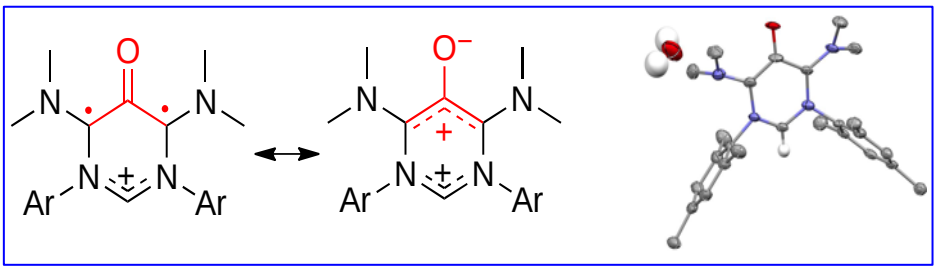

Figure 3: Equilibrium between dicationic and diradical conformations.

- We also designed highly reactive, but handle-able, dioxolyliums cations, which provided an opportunity for the first experimental study of dioxolyl radicals.

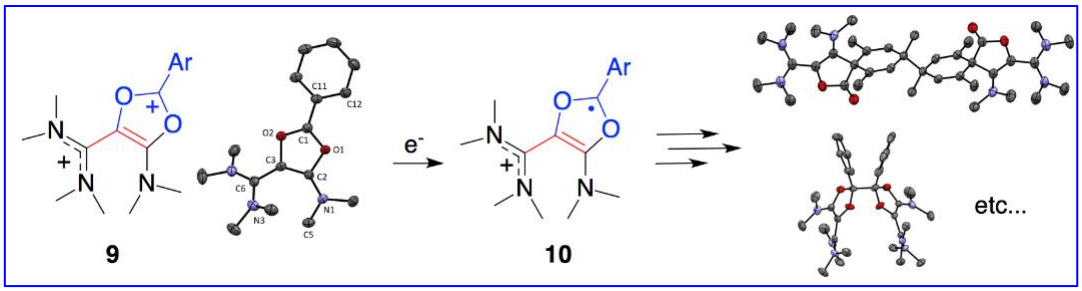

Figure 4: evolution of the dioxolium cation to reactive dioxolyl radicals and final reaction products.

♠ **Stable di- and tri-coordinated carbon(II) supported by an electron-rich β-diketiminate ligand,** Vianney Regnier, Yoan Planet, Curtis E. Moore, Jacques Pecaut, Christian Philouze, David Martin, Angew. Chem. Int. Ed. **2017,** *56*, 1031-1035.

♠ **Synthesis of dicationic dioxolium salts and their fate upon one-electron reduction**, Marc Devillard, Vianney Regnier, Jacques Pecaut, David Martin, *en préparation*

Semiconducting nanocrystals for biological applications

Coll. INAC/SyMMES

Cadmium-free quantum dots or fluorescent semiconductor nanocrystals are very promising candidates for use as biological probes due to their low toxicity. Their emissions can be tuned from the visible to the near-infrared region by modulating the size and composition of the nanoparticles. These quantum dots are generally protected by a high band gap material such as ZnS which serves also at improving the photophysical properties by passivating surface defects. This passivation with a shell material leads to an increase in photoluminescence as well as increased stability.

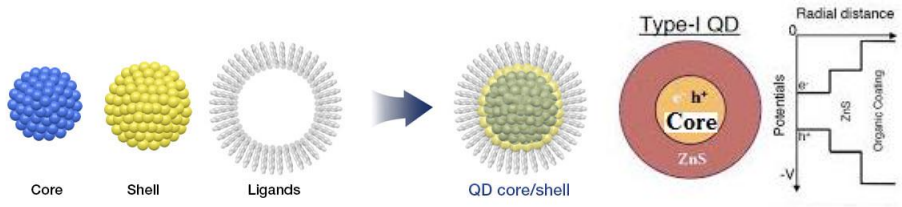

Figure 5: Representation of the quantum dots at different levels: core, shell and core@shell with ligands

The material studied here is the quaternary compound CuIn(S,Se). Core quantum dots of this material were synthesized in organic solution and a shell was grown to improve photoluminescence. Thus, we obtained core CuIn(S,Se) quantum dots and the core-shell counterparts CuIn(S,Se)@ZnS that emit in the near-infrared region.

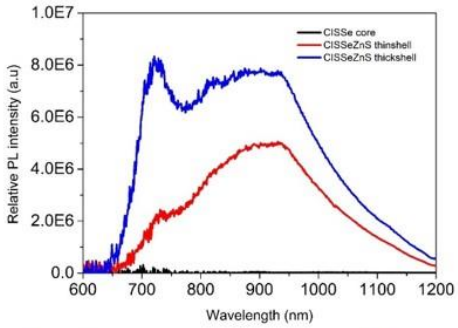

Figure 6: Photoluminescence spectra of the core, core-thin shell and core thick-shell taken at an excitation wavelength of 450 nm.

Photoluminescence was done on the core and core-shell quantum dots to check whether shell growth was efficient. The latter can be confirmed if there is an increase in photoluminescence intensity after passivation with ZnS. Figure 5 below shows that there is indeed an increase in PL intensity after shell growth. The core QDs are initially very poor emitters but upon shell growth, the PL emission increases drastically. This is a good indication that surface defects have been well passivated. It can be noted also that the spectra after shell growth show several maxima contrary to the core PL spectrum. The presence of several maxima could indicate that the QD solution contain particles of different sizes with different emission wavelengths.

Next, XRD was performed on the different quantum dots to verify the crystalline phase as well as the average size of the particles (see figure 7). The chalcopyrite phase (ICDD 04-020-4201) was found to be the best match for the compound CuIn(S,Se), as expected. If we look closely at the different diffractograms, we can see that there is a slight shift to higher angles from core to core@shell. The peaks are also more asymmetrical in the case of the core@shell compared to the core QDs.

The size of the QDs before and after shell growth were checked by the Scherrer formula, neglecting strain effect. The core QDs were found to be ~5.5-6 nm and the core@shell around 4-5 nm which is surprising. We would expect the core@shell QDs to be larger than the core QDs alone because the PL measurements showed that the surface was well passivated, indicating the presence of ZnS.

Hence, TEM measurements were done to investigate the size and morphology of the QDs. The core CuIn(S,Se) quantum dots appear to be pyramidal shaped and very monodisperse with a size between 6-7 nm, in good agreement with XRD. After shell growth. the QDs become very polydisperse but maintain their pyramidal shape. The size ranges between 4-12 nm, with a size mainly ~4-6 nm. This polydispersity confirms that the different sizes are responsible for the several maxima on the PL spectra after shell growth. The average value of the particle size obtained with XRD also shows that the majority of the core@shell particles are smaller than the core particles.

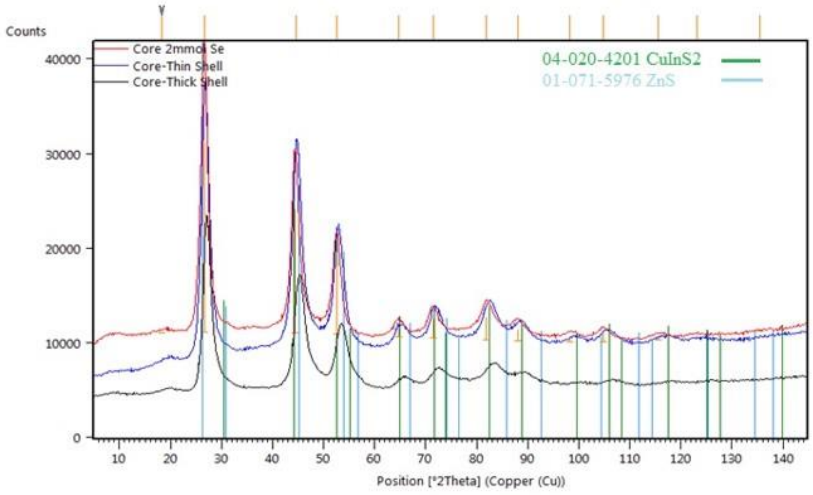

Figure 7: X-ray diffractograms obtained for different types of CuIn(S,Se) core based quantum dots (red: core only; blue: thin ZnS shell; black: thick ZnS shell).

Conclusion:

The three characterization techniques (XRD, TEM, and Photoluminescence) combined together were useful to show that the core synthesis was successful but not so much for the core@shell. Ideally, the size distribution should remain narrow after shell growth and a thick shell should lead to a larger shift to higher angles in the peak positions of the XR-diffractogram. We saw with XRD and TEM that the shell grown was not thick and only a few core@shell QDs were larger than the core. Size determination with Scherrer was already a good indication of the polydispersity of the sample. These results lead us to better understand the core@shell synthesis and the parameters that could affect dispersity (purity of core QDs solution, injection rate of shell precursors, temperature ramp).

Material synthesis / structuration

Growth Mechanism and Surface State of $CuInS_2$ Nanocrystals Synthesized with Dodecanethiol

Coll. INAC/SyMMES

Ternary metal chalcogenide nanocrystals (NCs) $M^+M^{3+}E^2$ (M^+ = Cu, Ag; M^{3+} = In, Fe; E = S, Se) have drawn tremendous research interest in the past decade, triggered by the discovery of their appealing optical properties. Going from binary to ternary (or multinary) systems opened many novel perspectives, enabled by the large scope of materials to be explored in the form of colloidal NCs for the first time. In these compounds, the optical and electronic properties can be tuned not only with the size and surface chemistry of the NCs but also by changing their composition. Of considerable importance is also the possibility to develop materials showing visible or near-infrared absorption/emission without relying on the use of toxic heavy metals such as Cd, Pb, or Hg. $CuInS_2$ (CIS)

NCs are the most widely studied representatives of this family as they can be easily prepared with good size control and in high yield by reacting the metal precursors (copper iodide and indium acetate) in dodecanethiol (DDT). Despite the widespread use of this synthesis method, both the reaction mechanism and the surface state of the obtained NCs remain elusive. We performed in situ X-ray diffraction using synchrotron radiation to monitor the pre- and postnucleation stages of the formation of CIS NCs. SAXS measurements showed that the reaction intermediate formed at 100 °C presents a periodic lamellar structure with a characteristic spacing of 34.9 Å. WAXS measurements performed after nucleation of the CIS NCs at 230 °C demonstrated the dependence of the growth kinetics on the degree of precursor conversion achieved in the initial stage at 100 °C.

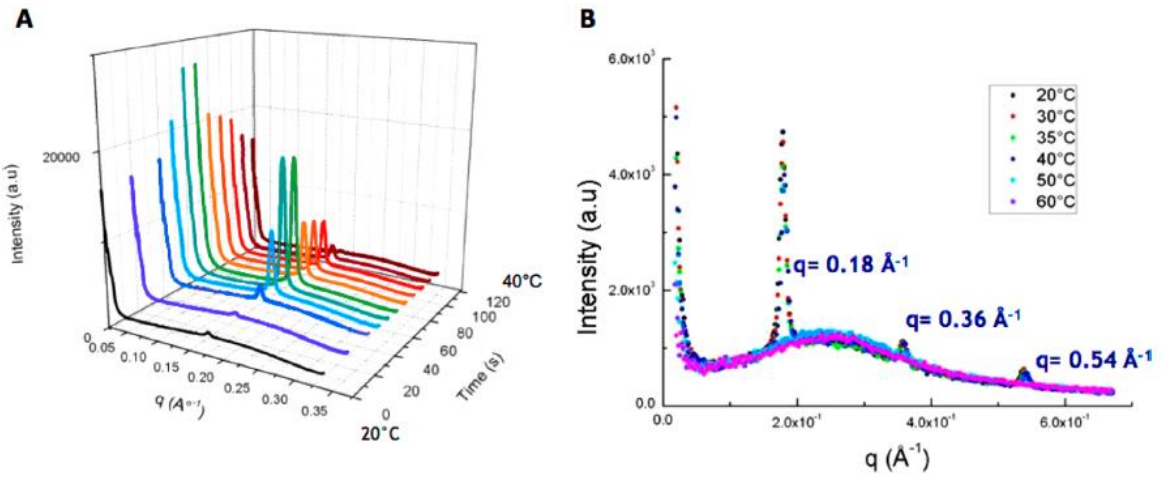

Figure 1: (A) Synchrotron in situ SAXS measurements performed during the heating of the CIS precursor solution in a glass capillary from 20 to 40°C within 2 min. The solution was preheated to 100 °C for 60 min before transferring it into the capillary). (B) Laboratory SAXS measurements at different temperatures on the same type of sample.

NC formation requires the cleavage of S−C bonds. This study revealed by means of combined 1D and 2D proton and carbon NMR analyses that the generated dodecyl radicals lead to the formation of a new thioether species R−S−R. The latter is part of a ligand double layer, which consists of dynamically bound dodecanethiolate ligands as well as of head-to-tail bound R−S−R molecules. This ligand double layer and a high ligand density (3.6 DDT molecules per nm2) are at the origin of the apparent difficulty to functionalize the surface of CIS NCs obtained with the DDT method.

♠ **Growth Mechanism and Surface State of CuInS2 Nanocrystals Synthesized with Dodecanethiol**, M. Gromova, A. Lefrançois, L. Vaure, F. Agnese, D. Aldakov, A. Maurice, D. Djurado, C. Lebrun, A. de Geyer, T. U. Schülli, S. Pouget, and P. Reiss**.** *J. Am. Chem. Soc. 2017, 139, 15748−15759*

Single crystal quality checking using X-ray Laue diffraction

INAC/PHELIQS/IMAPEC

Many crystal growth experiments were driven in IMAPEC elaboration laboratory, and have necessitated single grain confirmation and / or crystallographic matrix orientation determination. Those investigations were done after a first step of phase checking using X-ray powder diffraction.

Different systems were studied using flux technique and chemical vapor transport techniques giving rise to millimetric faceted crystals: intermetallics compounds $CeAg_2Si_2$ and MnSi, Mott insulators spinels GaV_4S_8, GeV_4S_8…

Many crystal growths were performed with the travelling solvent floating zone technique, using an image furnace, giving large crystals (volume ~ cm^3), typically cylindrical rod of diameter 6 to 8 mm with a length from 5 to 9 cm. Different systems of magnetocaloric garnets were investigated: $Dy_3Ga_5O_{12}$, $Yb_3Ga_5O_{12}$, $Gd_3Ga_5O_{12}$. Large single grains of fluoride systems, $GdLiF_4$ and $ErLiF_4$ have been also elaborated using Bridgman technique and were characterized with Laue X ray technique.

Other systems were investigation for their interest in the study of superconductivity such as Uranium compounds UBe_{13} and UTe_2.

Large single grains of neodymium boron magnets $Fe_2Nd_{14}B$ were also successfully grown from Czochralski technique for a collaboration with LITEN.

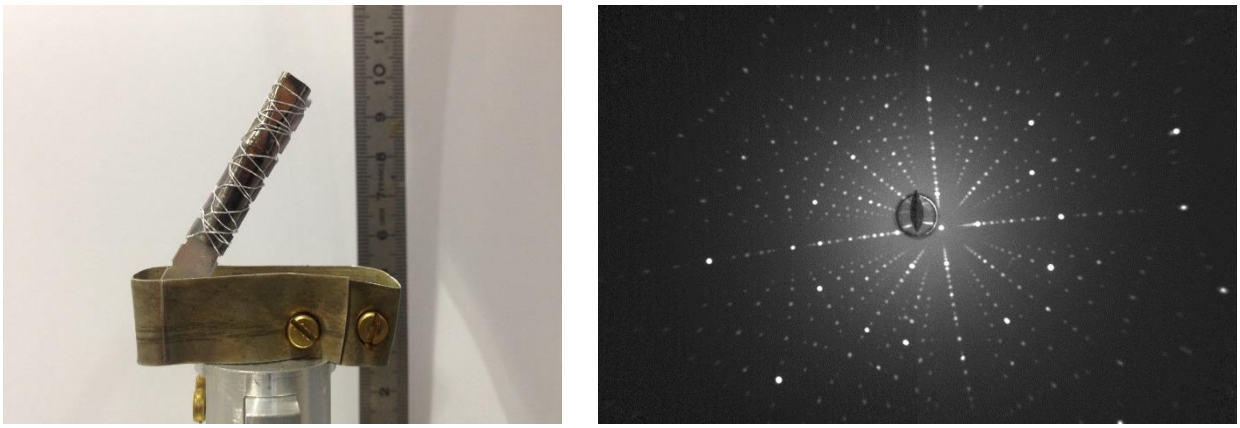

(a) *(b)*

Figure 2: (a) *$Nd_2Fe_{14}B$ large single crystal installed with a specific orientation for a neutron scattering experiment. (b) UBe_{13} large single crystal indexation using Orient Express*

Mott insulator compounds: new materials for resistive memory (RRAM)

INAC/PHELIQS/IMAPEC, LETI/DCOS/SCME

Resistive Random Access Memories (RRAM) use the large variation of resistance of a device to store 2 states of information. In several materials this change can be non-volatile, which is a strong asset for “low power” electronics.

In resistive memories based on Mott insulators, a non-volatile conductive filament is formed or disrupted in the insulating state by a voltage pulse. The mechanism could be mainly electronic, i.e. without displacement of chemical species. The main arguments supporting this assumption are the scaling of the threshold field (E_{th}) for resistive switching with the Mott insulating gap, following the same power-law as for electronic avalanche phenomena, and the 3 to 4 orders of magnitude smaller value of E_{th} compared to dielectric RRAM. Moreover, the existence of a thermodynamically stable conducting and insulating state, open the door to a resistive switching of bulk materials.

In this context, a fundamental study of the Mott-insulator mechanism in a selected family of spinel chalcogenides compounds AM_4X_8 (A = Ga, Ge / M = V, Nb, Ta… / X = S, Se) was initiated in 2015. First we focused on the crystal growth of GaV_4S_8, GeV_4S_8, GeV_4Se_8 compounds by chemical vapor transport, in order to study the metal-insulator transition. In a second part we worked on the elaboration of sulfide ceramic sputtering targets for thin films deposition using INAC-SPINTEC or LETI equipment. Each growth or steps of elaboration were checked by X ray powder diffractometer. (Julia MOKDAD thesis on GaV_4S_8 in IMAPEC group / September 2018-2021).

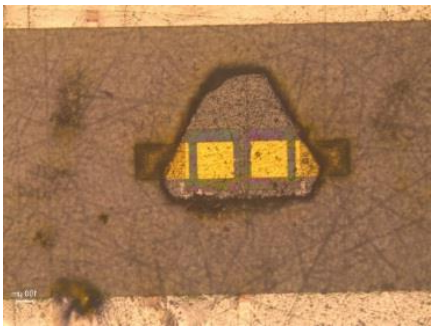

Figure 5: GaV_4S_8 single crystal obtained by chemical vapor transport using iodine as travelling agent, with gold electrodes deposed on its oriented surface for "Mott memory" behavior study (Julia MOKDAD).

Crystal growth and orientation of large single crystals of UO_2 compounds in collaboration with DEN - CEA Cadarache.

INAC/PHELIQS/IMAPEC and DEN – CEA Cadarache

The growth of large UO_2 crystals by chemical vapor transport is a new collaboration with DEN Cadarache (with a PhD thesis 2018-2021). The aim of the study being the growth of large UO_2 single grains, indexed and oriented before cutting, so as to produce specific grain boundaries elaborated by thermal diffusion gluing. The mechanical properties of those grain boundaries will be investigated to feed theoretical models dedicated to the safety of nuclear fuels.

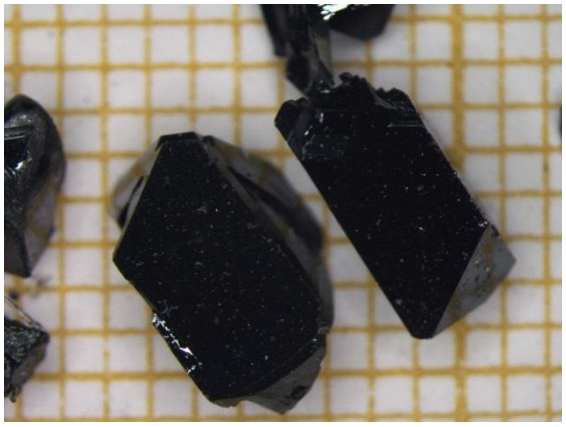

Figure 7: UO_2 large single obtained by chemical vapor transport.

Magnetocaloric and luminocaloric materials: rare earth garnets for 1K - 4K adiabatic refrigeration and rare earth lithium fluorides for optical cooling (bio medical research – CLINATEC).

INAC/PHELIQS/IMAPEC and CLINATEC
INAC/PHELIQS and INAC/SBT

Several magnetocaloric materials were studied in order to optimize their magnetic properties. We spent efforts on the synthesis of ceramics and crystal growth of:

- rare earth garnets $Dy_3Ga_5O_{12}$, $Gd_3Ga_5O_{12}$, $Yb_3Ga_5O_{12}$,
- pyrochlores $Tb_2Ti_2O_7$, $Er_2Ti_2O_7$
- fluorides $GdLiF_4$ and $ErLiF_4$.

Phase purity, crystal quality and cell parameters have to be checked at each steps of elaboration using X-ray powder diffractometer. Those materials were also controlled using scanning electronic microscopy and characterized with PPMS (for specific calorimetry) and MPMS (for magnetization). The final aim is to compare their magnetocaloric potential at low temperatures (1K – 4K).

A new material research project in collaboration with CLINATEC was also started to provide small high quality single crystals of $YLiF_4$ doped with rare earth Yb. Such luminocaloric material stimulated with a laser could allow refrigeration from room temperature down to 155 K. The aim of the CLINATEC project named EPICOOL is the development of small refrigerating biocompatible modules able to be inserted in human brain to fight deep epileptic crisis. Single crystals quality and purity needs to be control to ensure a very low Iron content.

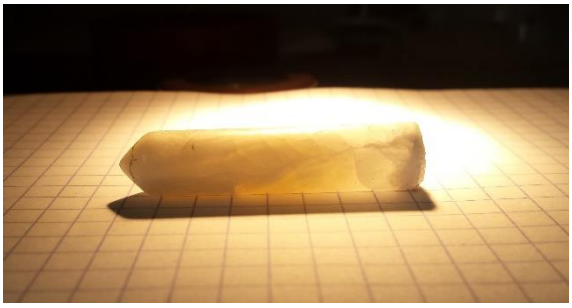

Figure 6: Bridgman growth of $YLiF_4$ crystals doped with Yb.

Synthesis of pseudo-boehmite from the wasted aluminium salts resulting from aluminium etching.

INAC/PHELIQS/SINAPS

Electrochemical etching of aluminium foil is a widely used technique for microstructuring the foil for capacitor anode purposes. However, this technique uses acid bath that is increasingly polluted via dissolved aluminum. This resultS in aluminum salt and a loss of acidity, an issue that is solved via adding new acid bath clean bath. However, the polluted bath needs to be valorized, since its acidity doesn't allow to be recycled through a wastewater treatment plant due to environmental norms and protections.

The study is about valorization of the wasted aluminum salt and characterizing of the pseudo-boehmite phase coming from the synthesis by precipitation using such aluminum salt. The XRD characterization was used for distinguishing the different phases among the obtained powder.

XRD measurements wee done to distinguish phases among different samples, such as shown in figure 8.

XRD measurement allowed to adjust the process of synthesis of pseudo-boehmite to obtain a crystalline mono-phased pseudo-boehmite.

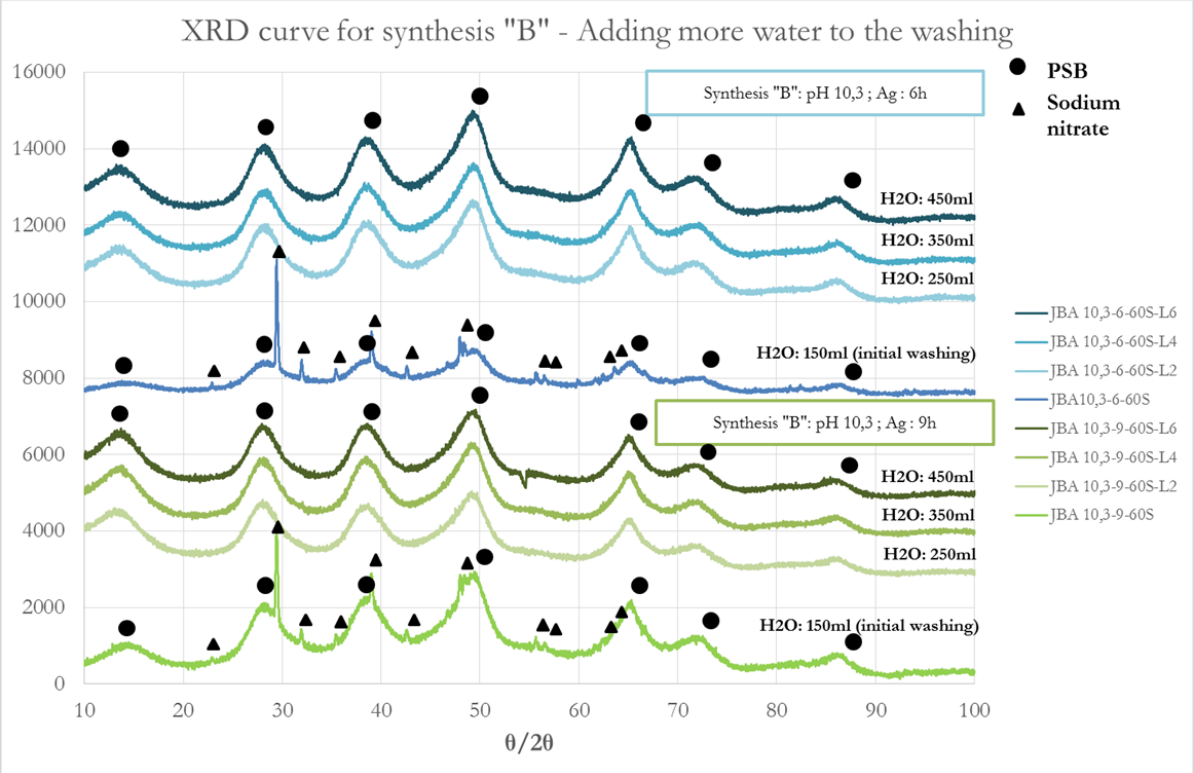

Figure 8 - Evolution of the presence of sodium nitrate as a function of the washing conditions for two different stirring times 6h (blue curves) and 9h (green curves).